

2017-11-06

Numerical algorithms for solving shallow water hydro-sediment-morphodynamic equations

Xia, C

<http://hdl.handle.net/10026.1/17704>

10.1108/ec-01-2016-0026

Engineering Computations

Emerald

All content in PEARL is protected by copyright law. Author manuscripts are made available in accordance with publisher policies. Please cite only the published version using the details provided on the item record or document. In the absence of an open licence (e.g. Creative Commons), permissions for further reuse of content should be sought from the publisher or author.



Numerical Algorithms for Solving Shallow Water Hydro-Sediment-Morphodynamic Equations

Journal:	<i>Engineering Computations</i>
Manuscript ID	EC-01-2016-0026.R2
Manuscript Type:	Research Article
Keywords:	Shallow water hydro-sediment-morphodynamic equations, Finite volume method, Well-balanced scheme, Coupled modelling, Fluvial processes

SCHOLARONE™
Manuscripts

1
2
3
4
5
6
7
8
9
10
11
12
13
14
15
16
17
18
19
20
21
22
23
24
25
26
27
28
29
30
31
32
33
34
35
36
37
38
39
40
41
42
43
44
45
46
47
48
49
50
51
52
53
54
55
56
57
58
59
60

1
2
3
4
5
6
7

Numerical Algorithms for Solving Shallow Water Hydro-Sediment-Morphodynamic Equations

Authors' info deleted for review

Engineering Computations

ABSTRACT

Purpose - The purpose of this paper is to present a fully conservative numerical algorithm for solving the coupled shallow water hydro-sediment-morphodynamic equations governing fluvial processes, and also to clarify the performance of a conventional algorithm, which redistributes the variable water-sediment mixture density to the source terms of the governing equations and accordingly the hyperbolic operator is rendered similar to that of the conventional shallow water equations for clear water flows.

Design/methodology/approach - The coupled shallow water hydro-sediment-morphodynamic equations governing fluvial processes are arranged in full conservation form, and solved by a well-balanced weighted surface depth gradient method along with a slope-limited centred scheme. The present algorithm is verified for a spectrum of test cases, which involve complex flows with shock waves and sediment transport processes with contact discontinuities over irregular topographies. The computational results of the conventional algorithm are compared with those of the present algorithm and evaluated by available referenced data.

Findings - The fully conservative numerical algorithm performs satisfactorily over the spectrum of test cases, and the conventional algorithm is confirmed to work similarly well.

Originality/value – A fully conservative numerical algorithm, without redistributing the water-sediment mixture density, is proposed for solving the coupled shallow water hydro-sediment-morphodynamic equations. It is clarified that the conventional algorithm, involving redistribution of the water-sediment mixture density, performs similarly well. Both algorithms are equally applicable to problems encountered in computational river modelling.

Keywords Shallow water hydro-sediment-morphodynamic equations, Finite volume method, Well-balanced scheme, Coupled modelling, Fluvial processes

Paper type Research paper

1
2
3 37 **1. Introduction**
4

5 38 The interactive processes of water flow, sediment transport and morphological evolution, as
6
7 39 influenced by both human activities and extreme natural events, constitute a hierarchy of physical
8
9
10 40 problems of significant interest in the fields of fluvial hydraulics and geomorphology. Great
11
12 41 efforts have been made to establish refined numerical models and to test the models over a range
13
14 42 of scales in laboratory and field experiments (Bellos et al. 1992, Fraccarollo and Toro 1995,
15
16 43 Capart and Young 1998, Fraccarollo and Capart 2002, Leal et al. 2006, Spinewine and Zech
17
18 44 2007).

19
20
21 45 The last several decades have witnessed rapid development and widespread applications of the
22
23 46 complete shallow water hydro-sediment-morphodynamic (SHSM) equations, which explicitly
24
25 47 accommodate the interactions between flow, sediment transport and bed evolution in a coupled
26
27 48 manner and adopt a non-capacity sediment transport approach based on physical perspectives
28
29 49 (Cao et al. 2004, 2016, 2017, Wu and Wang 2007). An increasing number of computational
30
31 50 studies in hydraulic engineering and geomorphological studies are based on the SHSM equations,
32
33 51 for example, dam-break floods over erodible bed (Cao et al. 2004, Wu and Wang 2007, Xia et al.
34
35 52 2010, Huang et al. 2012, 2014, 2015), coastal processes (Xiao et al. 2010, Kim 2015, Zhu and
36
37 53 Dodd 2015; Incelli et al. 2016; Briganti et al., 2016), watershed erosion processes (Kim et al.
38
39 54 2013), and turbidity currents (Hu et al. 2012, Cao et al. 2015), as well as rainfall-runoff processes
40
41 55 (Li and Duffy 2011).

42
43
44 56 The finite volume method (FVM) is one of the most promising methods for solving the SHSM
45
46 57 equations. Pivotal to this method is the determination of the numerical flux in cases where the
47
48 58 dependent variables may be steep-fronted or have discontinuous gradients. A series of numerical
49
50 59 schemes are available in this regard, such as the Harten-Lax-van Leer (HLL) scheme (Harten et al.
51
52 60 1983, Simpson and Castelltort 2006, Wu et al. 2012), the Harten-Lax-van Leer contact wave
53
54 61 (HLLC) scheme (Toro et al. 1994, Cao et al. 2004, Zhang and Duan 2011, Yue et al. 2015), the
55
56 62 Roe scheme (Roe 1981, Leighton et al. 2010, Xia et al. 2010, Li and Duffy 2011), and the slope
57
58
59
60

limited centred (SLIC) scheme (Toro 1999, Hu and Cao 2009, Qian et al. 2015, 2017). In recent years, well-balanced schemes (Qian et al. 2015, 2017, Liang 2010, Liang and Marche 2009, Aureli et al. 2008, Zhou et al. 2001) have been developed to improve the handling of source terms in numerical models and extend their applications to irregular topographies.

In practice, it is usual to manipulate the original SHSM equations into a form that eliminates the variable water-sediment mixture density on the left-hand-side (LHS) of the governing equations leading to the conventional numerical algorithm (CNA), which is an extension of existing numerical schemes for shallow water equations of clear water flows in both 1D (Cao et al. 2004, Wu and Wang 2008, Zhang and Duan 2011, Hu et al. 2014, Qian et al. 2015) and 2D modelling (Simpson and Castelltort 2006, Xia et al. 2010, Yue et al. 2015, Huang et al. 2012, 2014, 2015, Guan et al. 2014, 2015, 2016, Qian et al. 2017). However, it has so far remained poorly understood whether the equation manipulation could incur conservation errors due to the splitting of certain product derivatives by the chain rule and the reassignment of the split forms to flux gradient and source terms.

A fully conservative numerical algorithm (FCNA) is proposed herewith to directly solve the original SHSM equations, in which the mixture density is maintained on the LHS. Numerical fluxes and the bed slope source terms are estimated by the well balanced, weighted surface depth gradient method (WSDGM) version of the SLIC scheme (Aureli et al. 2008). The remainder of the paper is organized as follows. First, the governing equations are presented in the CNA and FCNA forms. Second, the numerical methods used to determine the numerical fluxes and source terms are outlined. Third, the CNA and FCNA are examined to show their capability of preserving quiescent flow, and then the FCNA is verified for several test cases, which involve complex flows with shock waves and also sediment transport processes with contact discontinuities over irregular topographies. The computational results of the CNA are also compared with those of the FCNA and evaluated using available observed data, analytical and

numerical solutions. Moreover, the relative run time and relative mass conservation errors of the two algorithms were discussed. Finally, conclusions are drawn from the present work.

2. Mathematical Model

2.1 Governing equations

The governing equations of SHSM models can be derived by directly applying the Reynolds Transport Theorem in fluid dynamics (Batchelor 1967, Xie 1990), or by integrating and averaging the three-dimensional mass and momentum conservation equations (Wu 2007). For ease of description, consider longitudinally one-dimensional flow over a mobile and mild-sloped bed composed of uniform (single-sized) and non-cohesive sediment. The governing equations comprise the mass and momentum conservation equations for the water-sediment mixture flow and the mass conservation equations, respectively, for sediment and bed material. These constitute a system of four equations and four physical variables (flow depth, depth-averaged velocity, sediment concentration and bed elevation), which can be written as

$$\frac{\partial(\rho h)}{\partial t} + \frac{\partial(\rho hu)}{\partial x} = -\rho_0 \frac{\partial z}{\partial t} \quad (1)$$

$$\frac{\partial(\rho hu)}{\partial t} + \frac{\partial}{\partial x} \left(\rho hu^2 + \frac{1}{2} \rho gh^2 \right) = \rho gh \left(-\frac{\partial z}{\partial x} - S_f \right) \quad (2)$$

$$\frac{\partial(hc)}{\partial t} + \frac{\partial(huc)}{\partial x} = E - D \quad (3)$$

$$\frac{\partial z}{\partial t} = -\frac{E - D}{1 - p} \quad (4)$$

where t = time; x = streamwise coordinate; h = flow depth; u = depth-averaged flow velocity in x direction; z = bed elevation; c = flux-averaged volumetric sediment concentration; g = gravitational acceleration; $S_f = n^2 u^2 / h^{4/3}$ = friction slope, and n = Manning roughness; p = bed

sediment porosity; E , D = sediment entrainment and deposition fluxes across the bottom boundary of flow, representing the sediment exchange between the water column and bed, which need to be quantified separately according to the specific test cases; $\rho = \rho_w(1-c) + \rho_s c$ = density of water-sediment mixture; $\rho_0 = \rho_w p + \rho_s(1-p)$ = density of saturated bed; and ρ_w , ρ_s = densities of water and sediment. Shape factors arising from depth-averaging manipulation in the preceding equations have been presumed to be equal to unity.

It is noted that the present model is physically coupled as the interactions between flow, sediment transport and bed evolution are explicitly accommodated. **Equally importantly**, the full set of the governing equations is numerically solved synchronously, which ensures numerical coupling. Meanwhile, the present model is based on a non-capacity approach (Cao et al. 2012, 2016, 2017), which determines sediment transport by incorporating the contributions of advection due to mean flow velocity and of the mass exchange with the bed. In contrast, capacity models (Canestrelli et al., 2010; Rosatti and Fraccarollo, 2006; Postacchini et al. 2012, 2014) presume the sediment concentration to be always equal to the transport capacity determined exclusively by the local flow and bed conditions, which are only conditionally applicable if sediment adaptation to capacity regime is fulfilled sufficiently rapidly and within an adequately short distance.

In order to facilitate mathematical manipulation, Eq. (4) is solved separately from Eqs. (1)-(3) as it is in essence an ordinary differential equation. Yet all variables are updated at each time step as shown in Section 2.4.1. It is physically justified due to the fact that bed deformation is solely determined by the local entrainment and deposition fluxes.

129

130 2.2 Equations in CNA form

In the CNA, Eqs. (1) and (2) are reformulated by eliminating the water-sediment mixture density on the LHS using Eqs. (3) and (4). Therefore, the hyperbolic operator is rendered similar to that of

the conventional shallow water equations for clear water flows. Accordingly, Eqs. (1), (2) and (3) are rewritten as

$$\frac{\partial \mathbf{U}}{\partial t} + \frac{\partial \mathbf{F}}{\partial x} = \mathbf{S}_b + \mathbf{S}_f \quad (5)$$

where \mathbf{S}_b = vector of bed slope source term components; \mathbf{S}_f = vector of other source terms; \mathbf{U} and \mathbf{F} = vectors as follows,

$$\mathbf{U} = \begin{bmatrix} h \\ hu \\ hc \end{bmatrix} \quad \mathbf{F} = \begin{bmatrix} hu \\ hu^2 + \frac{1}{2}gh^2 \\ huc \end{bmatrix} \quad (6a, b)$$

$$\mathbf{S}_b = \begin{bmatrix} 0 \\ -gh \frac{\partial z}{\partial x} \\ 0 \end{bmatrix} \quad \mathbf{S}_f = \begin{bmatrix} (E-D)/(1-p) \\ -ghS_f - \frac{(\rho_s - \rho_w)gh^2}{2\rho} \frac{\partial c}{\partial x} - \frac{(\rho_0 - \rho)(E-D)u}{\rho(1-p)} \\ E-D \end{bmatrix} \quad (6c, d)$$

It is noted that this treatment was first proposed and implemented by Cao et al. (2004) and has been widely used in computational river modelling (Simpson and Castelltort 2006, Wu and Wang 2007, Yue et al. 2008, Hu and Cao 2009, Xia et al. 2010, Huang et al. 2012, 2014, 2015, Li et al. 2014, Cao et al. 2015). More broadly, the idea behind this numerical strategy has also been applied to solve shallow water equations including an effective porosity parameter to represent the effect of small-scale impervious obstructions on reducing the available storage volume and effective cross section of shallow water flows (Cea and Vázquez-Cendón 2010).

2.3 Equations in FCNA form

In the FCNA, Eqs. (1)-(4) are solved directly, without first redistributing the water-sediment mixture density as in the CNA. If ρh and c/ρ are regarded as independent variables

respectively, Eqs. (1)-(3) can be written in the conservative form of Eq. (5), with vectors expressed in terms of variables $[\rho h \ u \ c / \rho]^T$, as follows,

$$\mathbf{U} = \begin{bmatrix} \rho h \\ \rho h u \\ \rho h \frac{c}{\rho} \end{bmatrix} \quad \mathbf{F} = \begin{bmatrix} \rho h u \\ \rho h u^2 + \frac{g}{2\rho} (\rho h)^2 \\ \rho h u \frac{c}{\rho} \end{bmatrix} \quad (7a,b)$$

$$\mathbf{S}_b = \begin{bmatrix} 0 \\ -\rho g h \frac{\partial z}{\partial x} \\ 0 \end{bmatrix} \quad \mathbf{S}_f = \begin{bmatrix} \rho_0 (E - D) / (1 - p) \\ -\rho g h S_f \\ E - D \end{bmatrix} \quad (7c,d)$$

2.4 Numerical scheme

2.4.1 Finite volume discretization

Implementing the finite volume discretization along with the operator-splitting method for Eq. (5), one obtains (Aureli et al. 2008, Hu et al. 2012, Hu et al. 2015, Qian et al. 2015)

$$\mathbf{U}_i^* = \mathbf{U}_i^n - \frac{\Delta t}{\Delta x} (\mathbf{F}_{i+1/2}^n - \mathbf{F}_{i-1/2}^n) + \Delta t \mathbf{S}_{bi} \quad (8)$$

where Δt = time step; Δx = spatial step; i = spatial node index; n = time node index; $\mathbf{F}_{i+1/2}$ = inter-cell numerical flux at $x = x_{i+1/2}$; and \mathbf{U}_i^* = the predicted conserved variables. The ordinary differential equations constituted by the source terms are solved using the second-order Runge–Kutta (RK) method (Gottlieb and Shu 1998)

$$\mathbf{U}_i^{(1)} = \mathbf{U}_i^* + \Delta t \mathbf{S}_f(\mathbf{U}_i^*) \quad (9a)$$

$$\mathbf{U}_i^{n+1} = \frac{1}{2} \mathbf{U}_i^* + \frac{1}{2} \mathbf{U}_i^{(1)} + \frac{1}{2} \Delta t \mathbf{S}_f(\mathbf{U}_i^{(1)}) \quad (9b)$$

The bed deformation is updated by the discretization of Eq. (4) in the same way as Eq. (9)

$$z_i^{(1)} = z_i^n + \Delta t \frac{(D-E)_i^*}{(1-p)} \quad (10a)$$

$$z_i^{n+1} = \frac{1}{2} z_i^n + \frac{1}{2} z_i^{(1)} + \frac{1}{2} \Delta t \frac{(D-E)_i^{(1)}}{(1-p)} \quad (10b)$$

For numerical stability, the time step satisfies the Courant–Friedrichs–Lewy (CFL) condition

$$\Delta t = \frac{C_r}{\lambda_{\max} / \Delta x} \quad (11)$$

where C_r is the Courant number and $C_r < 1$; and λ_{\max} is the maximum celerity computed from the Jacobian matrix $\partial \mathbf{F} / \partial \mathbf{U}$.

2.4.2 Well-balanced version of the SLIC scheme

Unlike certain well-balanced numerical schemes which directly adopt the water surface elevation as a flow variable in their rearranged SHSM equations (Rogers et al. 2003, Liang and Borthwick 2009, Liang and Marche 2009, Huang et al. 2012, 2014, Qian et al. 2015, 2016), the present model maintains the original equations, with the water depth variable evaluated from a weighted average of the slope limited water depth and water surface elevation (Zhou et al. 2001, Aureli et al. 2008, Hu et al. 2012) in the framework of the SLIC scheme that results from replacing the Godunov flux by the FORCE flux in the MUSCL-Hancock scheme (Toro 2001). The original SLIC scheme (Toro 2001, Aureli et al. 2004) is termed a depth-gradient method (DGM) version because it uses the spatial gradient of the water depth for the interpolation, and is robust and stable for cases involving high gradient in water level provided the bathymetry has small gradient. The scheme is also capable of tracking the motion of wetting and drying fronts above a threshold flow depth h_{lim} as discussed in Section 2.4.3. However, when the bed topography is irregular and has large spatial gradient, the DGM version may not reproduce the exact solution for stationary flows (i.e., it does not satisfy the exact *C-property* [Bermudez and Vazquez 1994]) because of the imbalance between the bed slope source term and flux gradient. The *C-property* can be instead

satisfied by the surface gradient method (SGM) proposed by Zhou et al. (2001), which is preferable for cases when small gradient in water level occurs alongside high gradient in water depth. However this method still has certain limitations in the treatment of the wetting and drying fronts that may lead to unphysical results (Aureli et al. 2008). To exploit the advantages of both DGM and SGM, following Aureli et al. (2008), the well-balanced WSDGM version of the SLIC scheme (Figure 1) is employed herein to estimate the numerical fluxes as well as the bed slope source term in Eq. (8). This method is similar to Hu et al. 2015, but it is necessary to note that their model is decoupled and capacity based, which is in contrast to the present model that explicitly accommodates the interactions between flow, sediment transport and bed evolution in a coupled manner and adopts a non-capacity sediment transport approach.

Step 1: Data reconstruction

For ease of description, a new vector of variables \mathbf{Q} is introduced, with $\mathbf{Q}_{CNA} = [h \quad hu \quad hc \quad \eta \quad z]^T$ and $\mathbf{Q}_{FCNA} = \left[\rho h \quad \rho hu \quad \rho h \frac{c}{\rho} \quad \rho \eta \quad \rho z \right]^T$ indicating the conventional and fully conservative algorithms respectively, where $\eta = h + z$ is the water surface elevation. The first four boundary extrapolated variables $\mathbf{Q}_{i+1/2}^L$ and $\mathbf{Q}_{i+1/2}^R$ are evaluated at the left and right sides of interface $x = x_{i+1/2}$ to achieve second-order accuracy in space.

$$\mathbf{Q}_{i+1/2}^L = \mathbf{Q}_i^n + \varphi_{i-1/2}^L \frac{\mathbf{Q}_i^n - \mathbf{Q}_{i-1}^n}{2} \quad (12a)$$

$$\mathbf{Q}_{i+1/2}^R = \mathbf{Q}_{i+1}^n - \varphi_{i+3/2}^R \frac{\mathbf{Q}_{i+2}^n - \mathbf{Q}_{i+1}^n}{2} \quad (12b)$$

where φ = slope limiter, which is a function of the ratios $r^{L,R}$ of variables \mathbf{Q} . Here the Minmod limiter is used, which reads

$$\varphi(r) = \begin{cases} \min(r, 1) & \text{if } r > 0 \\ 0 & \text{if } r \leq 0 \end{cases} \quad (13)$$

211 with

$$212 \quad r_{i-1/2}^L = \frac{Q_{i+1}^n - Q_i^n}{Q_i^n - Q_{i-1}^n} \quad r_{i+3/2}^R = \frac{Q_{i+1}^n - Q_i^n}{Q_{i+2}^n - Q_{i+1}^n} \quad (14a, b)$$

213 The last elements of $\mathbf{Q}_{i+1/2}^L$ and $\mathbf{Q}_{i+1/2}^R$ are evaluated at the interface $x = x_{i+1/2}$, such that,

$$214 \quad \mathbf{Q}_{i+1/2}^L(5) = \mathbf{Q}_{i+1/2}^R(5) = \frac{1}{2}(\mathbf{Q}_i^n(5) + \mathbf{Q}_{i+1}^n(5)) \quad (15)$$

215 The first elements of $\mathbf{Q}_{i+1/2}^L$ and $\mathbf{Q}_{i+1/2}^R$ are updated by a weighted average of boundary
216 extrapolated values derived from MUSCL DGM and SGM extrapolations as follows,

$$217 \quad \mathbf{Q}_{i+1/2}^L(1) = \phi \mathbf{Q}_{i+1/2}^L(1) + (1 - \phi) [\mathbf{Q}_{i+1/2}^L(4) - \mathbf{Q}_{i+1/2}^L(5)] \quad (16a)$$

$$218 \quad \mathbf{Q}_{i+1/2}^R(1) = \phi \mathbf{Q}_{i+1/2}^R(1) + (1 - \phi) [\mathbf{Q}_{i+1/2}^R(4) - \mathbf{Q}_{i+1/2}^R(5)] \quad (16b)$$

219 where ϕ = weighting factor between the DGM and SGM with $0 \leq \phi \leq 1$, which is specified as a
220 function of the Froude number Fr ,

$$221 \quad \phi = \begin{cases} 0.5 \left[1 - \cos \left(\frac{\pi Fr}{Fr_{lim}} \right) \right] & 0 \leq Fr \leq Fr_{lim} \\ 1 & Fr > Fr_{lim} \end{cases} \quad (17)$$

222 where Fr_{lim} is an upper limit beyond which a pure DGM reconstruction is performed. In this
223 paper, $Fr_{lim} = 2.0$ is adopted according to Aureli et al. (2008).

224 Boundary extrapolated vectors $\mathbf{Q}_{i+1/2}^L$ and $\mathbf{Q}_{i+1/2}^R$ are used to update the vectors of conserved
225 variables of the governing equations as follows,

$$226 \quad \mathbf{U}_{i+1/2}^L = [\mathbf{Q}_{i+1/2}^L(1) \quad \mathbf{Q}_{i+1/2}^L(2) \quad \mathbf{Q}_{i+1/2}^L(3)]^T \quad (18a)$$

$$227 \quad \mathbf{U}_{i+1/2}^R = [\mathbf{Q}_{i+1/2}^R(1) \quad \mathbf{Q}_{i+1/2}^R(2) \quad \mathbf{Q}_{i+1/2}^R(3)]^T \quad (18b)$$

228 **Step 2:** Evolution of extrapolated variables

The boundary extrapolated conserved variables are further evolved over $\Delta t / 2$ to achieve second-order accuracy in time. In order to satisfy the *C-property* when WSDGM is adopted, the contribution due to gravity must be included.

$$\bar{\mathbf{U}}_{i+1/2}^L = \mathbf{U}_{i+1/2}^L - \frac{\Delta t / 2}{\Delta x} [\mathbf{F}(\mathbf{U}_{i+1/2}^L) - \mathbf{F}(\mathbf{U}_{i-1/2}^R)] + \frac{\Delta t}{2} \mathbf{S}_{bi} \quad (19a)$$

$$\bar{\mathbf{U}}_{i+1/2}^R = \mathbf{U}_{i+1/2}^R - \frac{\Delta t / 2}{\Delta x} [\mathbf{F}(\mathbf{U}_{i+3/2}^L) - \mathbf{F}(\mathbf{U}_{i+1/2}^R)] + \frac{\Delta t}{2} \mathbf{S}_{bi+1} \quad (19b)$$

where \mathbf{S}_{bi} in Eqs. (19a) and (19b) are discretized using central-differences with extrapolated variables taken from Step 1 and $z_{i+1/2} = (z_{i+1} + z_i) / 2$.

$$\mathbf{S}_{bi} = \begin{bmatrix} 0 \\ -g [\mathbf{U}_{i+1/2}^L(1) + \mathbf{U}_{i-1/2}^R(1)] (z_{i+1/2} - z_{i-1/2}) / (2\Delta x) \\ 0 \end{bmatrix} \quad (20)$$

Step 3: Numerical fluxes and bed slope source term

The numerical fluxes are estimated by the FORCE (first-order centred) approximate Riemann solver, which is an average of the Lax–Friedrichs flux \mathbf{F}^{LF} and the two-step Lax–Wendroff flux \mathbf{F}^{LW2} (Toro 2001)

$$\mathbf{F}_{i+1/2} = (\mathbf{F}_{i+1/2}^{LW2} + \mathbf{F}_{i+1/2}^{LF}) / 2 \quad (21)$$

$$\mathbf{F}_{i+1/2}^{LW2} = \mathbf{F}(\mathbf{U}_{i+1/2}^{LW2}) \quad (22a)$$

$$\mathbf{U}_{i+1/2}^{LW2} = \frac{1}{2} (\bar{\mathbf{U}}_{i+1/2}^R + \bar{\mathbf{U}}_{i+1/2}^L) - \frac{1}{2} \frac{\Delta t}{\Delta x} (\mathbf{F}(\bar{\mathbf{U}}_{i+1/2}^R) - \mathbf{F}(\bar{\mathbf{U}}_{i+1/2}^L)) \quad (22b)$$

$$\mathbf{F}_{i+1/2}^{LF} = \frac{1}{2} (\mathbf{F}(\bar{\mathbf{U}}_{i+1/2}^R) + \mathbf{F}(\bar{\mathbf{U}}_{i+1/2}^L)) - \frac{1}{2} \frac{\Delta x}{\Delta t} (\bar{\mathbf{U}}_{i+1/2}^R - \bar{\mathbf{U}}_{i+1/2}^L) \quad (23)$$

Finally, the bed slope source term in Eq. (8) is computed using the evolved variables from Step 2,

$$\mathbf{S}_{bi} = \begin{bmatrix} 0 \\ -g[\bar{\mathbf{U}}_{i+1/2}^L(1) + \bar{\mathbf{U}}_{i-1/2}^R(1)](z_{i+1/2} - z_{i-1/2}) / (2\Delta x) \\ 0 \end{bmatrix} \quad (24)$$

In order to validate the well-balanced property of this numerical scheme, a quiescent-flow problem is considered here (i.e. $u \equiv 0$; $\eta \equiv \eta_0$). A fully SGM extrapolation is satisfied as the Froude number $Fr = 0$ and the weighting factor $\phi = 0$ according to Eqs. (16) and (17). If the cell i is wet as well as its adjacent cells $i-2, i-1, i+1$ and $i+2$ at the time node n , the values of the inter-cell variables after the reconstruction in Step1 can be obtained as,

$$\begin{aligned} \mathbf{U}_{i+3/2}^{L,R}(1) &= \psi(\eta_0 - z_{i+3/2}) & \mathbf{U}_{i+1/2}^{L,R}(1) &= \psi(\eta_0 - z_{i+1/2}) \\ \mathbf{U}_{i-1/2}^{L,R}(1) &= \psi(\eta_0 - z_{i-1/2}) & \mathbf{U}_{i-3/2}^{L,R}(1) &= \psi(\eta_0 - z_{i-3/2}) \end{aligned} \quad (25a)$$

$$\mathbf{U}_{i+3/2}^{L,R}(2) = \mathbf{U}_{i+1/2}^{L,R}(2) = \mathbf{U}_{i-1/2}^{L,R}(2) = \mathbf{U}_{i-3/2}^{L,R}(2) = 0 \quad (25b)$$

where $\psi = 1$ for CNA and $\psi = \rho$ for FCNA.

According to Step 2, the variables at inter-cells $i-1/2$ and $i+1/2$ after a time step of $\Delta t / 2$ evolution can be calculated as,

$$\bar{\mathbf{U}}_{i+1/2}^{L,R}(1) = \psi(\eta_0 - z_{i+1/2}) \quad \bar{\mathbf{U}}_{i-1/2}^{L,R}(1) = \psi(\eta_0 - z_{i-1/2}) \quad (26a)$$

$$\begin{aligned} \bar{\mathbf{U}}_{i+1/2}^L(2) &= 0 - \frac{\Delta t / 2}{\Delta x \psi} \left[\frac{1}{2} g \mathbf{U}_{i+1/2}^L(1)^2 - \frac{1}{2} g \mathbf{U}_{i-1/2}^R(1)^2 \right] \\ &\quad - \frac{\Delta t}{2} g [\mathbf{U}_{i+1/2}^L(1) + \mathbf{U}_{i-1/2}^R(1)] (z_{i+1/2} - z_{i-1/2}) / (2\Delta x) = 0 \\ \bar{\mathbf{U}}_{i+1/2}^R(2) &= 0 - \frac{\Delta t / 2}{\Delta x \psi} \left[\frac{1}{2} g \mathbf{U}_{i+3/2}^L(1)^2 - \frac{1}{2} g \mathbf{U}_{i+1/2}^R(1)^2 \right] \\ &\quad - \frac{\Delta t}{2} g [\mathbf{U}_{i+3/2}^L(1) + \mathbf{U}_{i+1/2}^R(1)] (z_{i+3/2} - z_{i+1/2}) / (2\Delta x) = 0 \\ \bar{\mathbf{U}}_{i-1/2}^L(2) &= 0 - \frac{\Delta t / 2}{\Delta x \psi} \left[\frac{1}{2} g \mathbf{U}_{i-1/2}^L(1)^2 - \frac{1}{2} g \mathbf{U}_{i-3/2}^R(1)^2 \right] \\ &\quad - \frac{\Delta t}{2} g [\mathbf{U}_{i-1/2}^L(1) + \mathbf{U}_{i-3/2}^R(1)] (z_{i-1/2} - z_{i-3/2}) / (2\Delta x) = 0 \\ \bar{\mathbf{U}}_{i-1/2}^R(2) &= 0 - \frac{\Delta t / 2}{\Delta x \psi} \left[\frac{1}{2} g \mathbf{U}_{i+1/2}^L(1)^2 - \frac{1}{2} g \mathbf{U}_{i-1/2}^R(1)^2 \right] \\ &\quad - \frac{\Delta t}{2} g [\mathbf{U}_{i+1/2}^L(1) + \mathbf{U}_{i-1/2}^R(1)] (z_{i+1/2} - z_{i-1/2}) / (2\Delta x) = 0 \end{aligned} \quad (26b)$$

Following Step 3, the inter-cell numerical fluxes at $i-1/2$ and $i+1/2$ are conducted. Therefore, the variables at the next time can be updated due to Eqs. (8) and (9) as follows, which shows the static flow is maintained.

$$\mathbf{F}_{i+1/2}^n = \mathbf{F}_{i+1/2}^{LF} = \mathbf{F}_{i+1/2}^{LW2} = \begin{pmatrix} 0 \\ \frac{1}{2} g \psi (\eta_0 - z_{i+1/2})^2 \end{pmatrix} \quad (27a)$$

$$\mathbf{F}_{i-1/2}^n = \mathbf{F}_{i-1/2}^{LF} = \mathbf{F}_{i-1/2}^{LW2} = \begin{pmatrix} 0 \\ \frac{1}{2} g \psi (\eta_0 - z_{i-1/2})^2 \end{pmatrix} \quad (27b)$$

$$\begin{aligned} \mathbf{U}_i^{n+1} = \mathbf{U}_i^n - \frac{\Delta t}{\Delta x} & \left[\begin{pmatrix} 0 \\ \frac{1}{2} g \psi (\eta_0 - z_{i+1/2})^2 \end{pmatrix} - \begin{pmatrix} 0 \\ \frac{1}{2} g \psi (\eta_0 - z_{i-1/2})^2 \end{pmatrix} \right] \\ & + \Delta t \left[\begin{pmatrix} 0 \\ -g [\psi (\eta_0 - z_{i+1/2}) + \psi (\eta_0 - z_{i-1/2})] (z_{i+1/2} - z_{i-1/2}) / (2\Delta x) \end{pmatrix} \right] = \mathbf{U}_i^n \end{aligned} \quad (28)$$

Figure 1. Definition sketch of the WSDGM version of the SLIC scheme

2.4.3 Wet-dry front

First, a special treatment is performed at a wet-dry front in order to satisfy the *C-property*. If the water surface of the wet cell is lower than the bed elevation of its adjacent dry cell, the bed elevation and water surface of the dry cell are set to be the water level of the wet cell temporarily only when computing the numerical flux. For example, if the cell i is wet while the adjacent cell $i+1$ is dry and $\eta_i < z_{i+1} = \eta_{i+1}$, then the latter is modified so that $z_{i+1} = \eta_{i+1} = \eta_i$, which ensures that the depth in the cell $i+1$ is still zero. After the evolution in Steps 1 and 2, the same inter-cell variables at $i+1/2$ can be obtained as Eq. (25) and (26) (i.e., $\bar{\mathbf{U}}_{i+1/2}^{L,R}(1) = \psi(\eta_0 - z_{i+1/2})$ and

1
2
3
4
5
6
7
8
9
10
11
12
13
14
15
16
17
18
19
20
21
22
23
24
25
26
27
28
29
30
31
32
33
34
35
36
37
38
39
40
41
42
43
44
45
46
47
48
49
50
51
52
53
54
55
56
57
58
59
60

$\overline{U}_{i+1/2}^{L,R}(2) = 0$). Then, the inter-cell numerical fluxes at $i + 1/2$ are computed as Eq. (27a) in order to maintain the static state at the cell i .

Second, a threshold flow depth h_{lim} is introduced because the occurrence of very small water depth may lead to instabilities in numerical simulations due to the possible infinite bed resistance, especially at wet–dry front. If the computed water depth is lower than the threshold value, the depth, velocity and sediment concentration are all set to be zero. The threshold flow depth is a model parameter and a value of $h_{lim} = 1 \times 10^{-6}$ is adopted in the present work.

3. Test Cases

A series of test cases are presented to verify the performance of the FCNA, accompanied by comparisons with the CNA using the same numerical scheme. The test cases include steady flow at equilibrium conditions over a steep bump (Aureli et al. 2008) (Case 1) to examine satisfaction of the *C-property*, a density dam break with two initial discontinuities without bed deformation (Leighton et al. 2010) (Cases 2), dam-break over erodible beds at prototype-scale (Cao et al. 2004) (Case 3) and laboratory-scale (Fraccarollo and Capart 2002) (Case 4), and landslide dam failure (Cao et al. 2011a) (Case 5). The spatial step Δx is set specifically for different cases and the time step Δt then obtained according to the CFL stability requirement of Eq. (11), as listed in Table I.

In Case 4, the flow depth temporal and spatial scales are so small that a relatively large frictional source term may lead to numerical instability even if the CFL condition is satisfied. Thus, according to Qian et al. (2015), a number of sub-time steps Δt_σ are deployed when updating the solutions to the next time step in Eq. (9). Table II summarizes the parameter values for the different test cases.

301 **Table I.** Spatial increment and Courant number used in test cases

Test case	1	2	3	4	5
Spatial step Δx (m)	0.05	0.02	10	0.005	0.04
Courant number C_r	0.95	0.95	0.95	0.95	0.95

302
303 **Table II.** Summary of test cases

Test case	Sediment density ρ_s (kg/m ³)	Water density ρ_w (kg/m ³)	Gravitational acceleration g (m/s ²)	Sediment diameter d (mm)	Manning roughness n	Sediment porosity p
1	2,650	1,000	9.8	N/A	0.0	N/A
2	0.5&2.0	1.0	1.0	N/A	0.0	N/A
3	2,650	1,000	9.8	8.0	0.03	0.4
4*	1,540	1,000	9.8	3.5	0.025	0.3
5*	2,650	1,000	9.8	0.8	0.012	0.4

304 Notes: * Cases using measured data.

305

306 To quantify the differences between FCNA and CNA, as well as the discrepancies between the
 307 simulations and available referenced data, the non-dimensional discrepancy is defined based on
 308 the L^1 norm.

$$309 \quad L_V = \frac{\sum abs(V_{CNA_i} - V_{FCNA_i})}{\sum abs(V_{CNA_i})} \times 100\% \quad (29)$$

$$310 \quad L_V^* = \frac{\sum abs(V_i - V_{*i})}{\sum abs(V_{*i})} \times 100\% \quad (30)$$

311 where V and V_* = the predicted and referenced variables, i.e., stage η , bed elevation z , velocity
 312 u and concentration c , with subscripts FCNA and CNA denoting corresponding algorithms;
 313 $L_{V(V=\eta, z, u, c)}$ is the L^1 norm used to compare the results of FCNA with those of CNA; and

314 $L^1_{V(V=\eta, z, u, c)}$ is the L^1 norm used to compare the predictions by FCNA and CNA with referenced
 315 data, i.e., analytical solutions for Case 1, referenced numerical solutions for Cases 2 and 3 and
 316 measured data for Cases 4 and 5.

317

318 3.1 Case 1: Steady flow at rest over a steep bump

319 To test whether or not the numerical algorithms satisfy the *C-property* over irregular topography,
 320 a frictionless channel $[-10 \text{ m} \leq x \leq 10 \text{ m}]$ is considered with its bed profile characterized by the
 321 presence of a steep bump, described as (Liska and Wendroff 1998)

$$322 \quad z(x) = \begin{cases} 0.8(1 - x^2/4) & -2 \text{ m} \leq x \leq 2 \text{ m} \\ 0 & \text{elsewhere} \end{cases} \quad (31)$$

323 Initially the flow is static and there is no water or sediment input at the inlet boundary. Two
 324 conditions of initial stage are considered. One has a stage of $\eta_0 = 1.0 \text{ m}$ (i.e., fully wet bed)
 325 referred to as Case 1a, while the other has a stage of $\eta_0 = 0.5 \text{ m}$ (i.e., with wet-dry interfaces),
 326 called Case 1b.

327 Figures 2 and 3 show the predicted stage and depth-averaged velocity profiles over the subdomain
 328 $[-3 \text{ m} \leq x \leq 3 \text{ m}]$ at $t = 1 \text{ h}$ obtained for the two initial conditions, using the FCNA and CNA.
 329 The initial steady, static equilibrium state is maintained by both algorithms, demonstrating that
 330 they are exactly well-balanced for cases with irregular topography irrespective of whether or not
 331 wet-dry interfaces are involved. The *C-property* can also be illustrated by $L^1_\eta = 0$ in Table III,
 332 indicating the computed stage is exactly the same as the analytical solution $\eta_* = \eta_0$ for both
 333 FCNA and CNA.

334

335 **Figure 2.** Case 1a: equilibrium stage and velocity profiles predicted by FCNA and CNA for initial
 336 stage of 1.0 m

Figure 3. Case 1b: equilibrium stage and velocity profiles predicted by FCNA and CNA for initial stage of 0.5 m

Table III. L_{η}^* for Case 1

L_{η}^* (%)	FCNA	CNA
Case 1a	0.0	0.0
Case 1b	0.0	0.0

3.2 Case 2: Density dam break with two initial discontinuities

Case 2 considers a density dam break in a channel with fixed horizontal bed, containing a central region of different density to that elsewhere in the channel. The channel is 100 m long and the region of different density is 1.0 m wide separated by two infinitesimally thin dams located at $x = 49.5$ and 50.5 m. Initially, the stage throughout the channel is 1.0 m, and the liquid densities in the central region bounded by the dam walls are $\rho_{in} = 0.5$ (Case 2a) and 2 kg/m^3 (Case 2b) with the initial interior concentration set to $c_{in} = 1$. Elsewhere the initial liquid density is set to $\rho_{out} = 1 \text{ kg/m}^3$ with initial concentration $c_{out} = 0$.

Figure 4 shows the good agreement of the stage and velocity profiles computed by Leighton et al. 2010 (referenced numerical solutions) with those by FCNA and CNA at $t = 30$ s. The corresponding concentration profiles predicted by the two algorithms are also displayed. Figures 5 and 6 show the temporal variations in stage, velocity and concentration at $x = 25, 50$ and 75 m (i.e. upstream of the first dam, at the mid-point between the dams, and downstream of the second dam) from FCNA and CNA. The predicted interactions between the denser liquid and less dense

liquid by FCNA and CNA are almost identical: the denser liquid moves inwards towards the centre of the channel, squeezing the less dense region upwards for $\rho_{in} = 0.5 \text{ kg/m}^3$, whilst for $\rho_{in} = 2 \text{ kg/m}^3$, the denser liquid falls under gravity, driving left and right shock-type bores into the adjacent less dense liquid (Fig. 4). Computed profiles of the temporal variations at selected sections for $\rho_{in} = 0.5$ and 2 kg/m^3 show opposite behaviour in water surface and velocity (Figs. 5 and 6) because the relative density ρ_{in} / ρ_{out} is less and greater than 1.0 respectively. Tables IV and V list the values obtained for L_v^* of stage and velocity at $t = 30 \text{ s}$ and L_v for Case 2 at selected instant and sections. Similar simulations between Leighton et al. 2010 and the two algorithms are illustrated by the values of L_v^* , within 5% for stage and 7% for velocity. L_η has slight differences and L_η has values close to zero, indicating negligible stage discrepancies between the two algorithms. The L_u and L_c values are within 3.5% and 0.05% respectively, limited discrepancies. Case 2 confirms that both FCNA and CNA provide acceptable solutions to the problems of dam break arising from discontinuous density gradients.

Figure 4. Case 2: computed stage, velocity and concentration profiles by FCNA and CNA and referenced stage and velocity profiles by Leighton et al. (2010) at $t = 30 \text{ s}$ for density dam break with two discontinuities for densities (a) $\rho = 0.5 \text{ kg/m}^3$ and (b) $\rho = 2 \text{ kg/m}^3$.

Figure 5. Case 2a: stage, velocity, and concentration time histories at locations (a) $x = 25 \text{ m}$, (b) $x = 50 \text{ m}$, and (c) $x = 75 \text{ m}$, predicted by FCNA and CNA for density dam break ($\rho_{in} = 0.5 \text{ kg/m}^3$) with two discontinuities.

Figure 6. Case 2b: stage, velocity, and concentration time histories at locations (a) $x = 25$ m, (b) $x = 50$ m, and (c) $x = 75$ m, predicted by FCNA and CNA for density dam break ($\rho_{in} = 2.0$ kg/m³) with two discontinuities.

Table IV. L_v^* for Case 2 at $t = 30$ s

Case	L_v^*	FCNA	CNA
Case 2a $\rho_{in} = 0.5$ kg/m ³	L_η^* (%)	4.50	4.50
	L_u^* (%)	6.67	6.73
Case 2b $\rho_{in} = 2$ kg/m ³	L_η^* (%)	2.48	2.49
	L_u^* (%)	4.44	5.85

Table V. L_v for Case 2 at selected instant and sections

Case	L_v	$t = 30$ s	$x = 25$ m	$x = 50$ m	$x = 75$ m
Case 2a $\rho_{in} = 0.5$ kg/m ³	L_η (%)	0.002	0.0008	0.01	0.01
	L_u (%)	1.65	0.26	N/A	0.56
	L_c (%)	0.04	N/A	0.002	N/A
Case 2b $\rho_{in} = 2$ kg/m ³	L_η (%)	0.02	0.016	0.02	0.015
	L_u (%)	3.25	3.26	N/A	0.07
	L_c (%)	0.016	N/A	0.00	N/A

3.3 Case 3: Dam-break over erodible beds of prototype scale

1
2
3
4
5
6
7
8
9
10
11
12
13
14
15
16
17
18
19
20
21
22
23
24
25
26
27
28
29
30
31
32
33
34
35
36
37
38
39
40
41
42
43
44
45
46
47
48
49
50
51
52
53
54
55
56
57
58
59
60

Case 3 is used to test the relative performance of FCNA and CNA in modelling the mobile bed hydraulics due to the instantaneous, full collapse of a dam. This test case was first proposed by Cao et al. (2004) for a dam break in a long channel at prototype scale, with the simulation being of relatively long duration. The dam is located at the centre of a 50-km-long channel and the mobile bed is composed of uniform and non-cohesive sediment. Initially, the bed is horizontal and the static water depths upstream and downstream of the dam are 40 m and 2 m respectively. The duration of the numerical simulations was such that they were concluded before forward and backward waves reached the downstream and upstream boundaries, so that the boundary conditions could be simply set according to the initial static states. The same empirical relationships are implemented for net sediment exchange flux as used by Cao et al. (2004).

Figures 7 and 8 compare the water surface and bed elevation computed by FCNA and CNA with those predicted by Cao et al. (2004) (i.e., referenced numerical solutions) at two times and two sections respectively. Longitudinal profiles of velocity and concentration at $t = 30$ s and 20 min (Fig. 7) and temporal variations of velocity and concentration at $x = 20$ and 30 km (i.e. 5 km upstream and downstream of the dam) (Fig. 8) from FCNA and CNA are also presented. It can be seen that FCNA and CNA both give very similar predictions of the dam break process as it evolves and the simulations agree well with the referenced stage and bed elevation ((a1) and (b1) in Figs. 7 and 8), with values of L_{η}^* and L_z^* within 1.5% and 7.5% in Table VI. The location of the hydraulic jump ((a1) and (b1) in Fig. 7) can be properly modelled by the FCNA as well as the abrupt fall in the free surface due to the existence of the contact discontinuity of sediment concentration ((a3) and (b3) in Fig. 7). It should be noted that the sharp concentration gradient at the wave front ((a3) and (b3) in Fig. 7) is modelled by the second term of the second component of Eq. (6d) by the CNA, whereas it is incorporated in the mixture density variation term ρh by the FCNA. The similar L_{η}^* values of FCNA and CNA and the small L_{η} values (within 1.5%) listed respectively in Tables VI and VII demonstrate that the discrepancies between FCNA and CNA are hardly distinguishable at the selected instants and sections.

Figure 7. Case 3: dam break over an erodible bed at prototype scale: profiles of water surface and bed elevation, velocity, and concentration computed by FCNA and CNA and referenced stage and bed elevation predicted by Cao et al. (2004) at times (a) $t = 30$ s and (b) $t = 20$ min.

Figure 8. Case 3: dam break over an erodible bed at prototype scale: time histories of water surface and bed elevation, velocity, and concentration computed by FCNA and CNA and referenced stage and bed elevation predicted by Cao et al. (2004) at locations (a) $x = 20$ km and (b) $x = 30$ km.

Table VI. L_v^* for Case 3 at selected instants and sections

L_v^*	$t = 30$ s	$t = 20$ min	$x = 20$ km	$x = 30$ km
L_η^* of FCNA (%)	1.02	1.20	1.64	3.39
L_z^* of FCNA (%)	7.48	4.75	4.18	2.40
L_η^* of CNA (%)	0.90	1.17	1.66	3.41
L_z^* of CNA (%)	7.07	5.11	4.23	2.65

Table VII. L_v for Case 3 at selected instants and sections

L_v	$t = 30$ s	$t = 20$ min	$x = 20$ km	$x = 30$ km
L_η (%)	0.004	0.069	0.18	0.18
L_z (%)	0.63	0.57	0.18	0.48
L_u (%)	0.50	0.18	0.04	0.21
L_c (%)	1.29	0.72	0.16	0.53

3.4 Case 4: Experimental dam-break over erodible beds

1
2
3
4
5
6
7
8
9
10
11
12
13
14
15
16
17
18
19
20
21
22
23
24
25
26
27
28
29
30
31
32
33
34
35
36
37
38
39
40
41
42
43
44
45
46
47
48
49
50
51
52
53
54
55
56
57
58
59
60

Laboratory experiments of dam break flow over a mobile bed reported in the literature include those of Capart and Young 1998, Fraccarollo and Capart 2002, Spinewine and Zech 2007, and Zech et al. 2008. Case 4, considered here, is that of Fraccarollo and Capart (2002) who conducted small-scale dam break tests in a channel 2.5 m long, 0.1 m wide and 0.35 m deep. The initial static water depths upstream and downstream of the dam were 0.1 m and 0 m respectively. In the numerical models, the boundary conditions are set to be the same as for Case 4. The net sediment exchange flux is determined following Cao et al. (2011b) with modification coefficients $\beta = 9$ and $\varphi = 3$. Tables I and II list the remaining model parameters.

Figure 9 shows measured and predicted stage and bed elevation profiles along a 2.5 m reach of the channel at times $t = 0.505$ and 1.01 s after the dam break. Figure 10 displays the corresponding velocity and concentration profiles. The agreement between the FCNA and CNA simulations and the experimental measurements is fairly good; the initial bore and rarefaction waves match well, though there is some slight discrepancy between the measured and predicted reflected wave that seems trapped as a hydraulic jump at the location of the original dam break. This wave reflects from the bed as it is eroded, and its magnitude is underestimated by the FCNA and CNA numerical models (both of which give almost identical results). The velocity and concentration profiles are both characterized by an abrupt fall in velocity and a sharp spike in concentration at the initial bore front as it propagates downstream. Figure 11 compares the FCNA and CNA predicted stage, bed elevation, velocity, and concentration time series at $x = -0.05$ and $x = 0.05$ m (0.05 m upstream and downstream of the initial dam respectively). The close agreement between the FCNA and CNA results is corroborated quantitatively in Table VIII by the values of L_η that are all within 2.5 %. Meanwhile, the FCNA and CNA results both display similar differences to the measured stage (as mentioned above) leading to values of L_η^* of 7.43% for FCNA and 7.41% for CNA at $t = 0.505$ s and 8.79% and 8.84% at $t = 1.01$ s, respectively. It is noted that the test case of Fraccarollo and Capart (2002) was also reproduced by Postacchini et al. (2012, 2014). Despite the similar results with those illustrated in Figure 9, their models were

essentially physically decoupled and a numerical coupling method was adopted in order to weakly couple hydrodynamics and morphodynamics. Moreover, based on the capacity assumption, they neglected the temporal and spatial variability of sediment transport. The discrepancies, however, between the results of Postacchini et al. (2012, 2014) and the present models are rather limited, which may be ascribed to the small temporal and spatial scales in this particular case. A more intensive investigation into the effects of the capacity assumption for sediment transport as compared against non-capacity modelling can be seen by Cao et al. (2011c), (2012), (2016) and Pelosi and Parker (2014). Overall, the results from Case 3 (involving large temporal and spatial scales) and Case 4 (involving experimental data at laboratory scale) help provide confidence in the FCNA as a model for highly unsteady shallow flows with shock waves and sediment transport.

Figure 9. Case 4: computed (FCNA and CNA) and measured (Fraccarollo and Capart, 2002) water surface and bed elevation profiles at (a) $t = 0.505$ s and (b) $t = 1.01$ s for a dam break over an erodible bed.

Figure 10. Case 4: computed (FCNA and CNA) velocity and concentration profiles at (a) $t = 0.505$ s and (b) $t = 1.01$ s for a dam break over an erodible bed.

Figure 11. Case 4: computed (FCNA and CNA) water surface, bed elevation, velocity, and concentration time series at (a) $x = -0.05$ m and (b) $x = 0.05$ m for a dam break over an erodible bed.

Table VIII. L_v^* and L_v for Case 4 at selected instants and sections

L_v^* or L_v	$t = 0.505$ s	$t = 1.01$ s	$x = -0.05$ m	$x = 0.05$ m
L_η^* of FCNA (%)	7.43	8.79	N/A	N/A
L_η^* of CNA (%)	7.41	8.84	N/A	N/A

L_{η} (%)	0.09	0.20	1.90	1.90
L_z (%)	1.36	1.25	1.92	1.66
L_u (%)	0.36	0.44	0.89	0.94
L_c (%)	1.35	2.21	1.45	1.77

3.5 Case 5: Flood flow due to landslide dam failure

Landslide dam failures involve wet-dry fronts propagating over irregular bed topography, and so constitute prime test cases by which to evaluate and compare the FCNA and CNA models in terms of their well-balanced properties and their treatment of wet-dry interfaces, in addition to shock capturing. Cao et al. (2011a) document results from a series of flume experiments on landslide dam breaches and subsequent flood wave propagation in a large-scale flume of dimensions 80 m \times 1.2 m \times 0.8 m and a fixed bed slope of 0.001. The experiments were implemented for different types of dams (i.e. with and without an initial breach) and dam material compositions in order to provide a unique, systematic set of measured data for validating numerical models of dam breaches and the resulting floods.

To demonstrate the performance of the FCNA, a uniform sediment case with no initial breach, i.e., F-case 15 (Cao et al. 2011a), is revisited here as Case 5. In this case, the dam was located at 41 m from the flume inlet, was 0.4 m high and had a crest width of 0.2 m. The initial upstream and downstream slopes of the dam were 1:4 and 1:5, respectively. The initial static water depths immediately upstream and downstream of the dam were 0.054 m and 0.048 m respectively. The inlet flow discharge was 0.025 m³/s⁻¹, and no sediment was present. A 0.15 m high weir was situated at the outlet of the laboratory flume, and so a transmissive condition was imposed at the downstream boundary of the numerical models. Following Cao et al. (2011b), the net sediment exchange flux is determined with modification coefficients $\beta = 9$ and $\varphi = 3$ for both FCNA and CNA.

Figure 12 shows the predicted and measured stage hydrographs at selected cross sections. For F-
case 15, cross-sections CS1 and CS5 are 22 m and 1 m upstream of the dam, whilst cross-sections
CS8 and CS12 are 13 m and 32.5 m downstream of the dam. The stage hydrographs computed by
FCNA and CNA are both in good agreement with the measured data from Cao et al. (2011a).
Figure 13 presents the predicted water surface and bed profiles along with the measured stage at
times $t = 670, 730$ (shortly after the erosion of the dam) and 900 s (nearly final state of the dam
failure). It is hard to say which algorithm better reproduces the processes of the dam failure as
both the simulations of FCNA and CNA match the measured data very well and the differences
between the results of the two algorithms are too subtle to distinguish. Echoing Figures 12 and 13,
the values of the L_η^* and L_η in Table IX provide further insight into the relative performances of
FCNA and CNA in comparison with the measured data. The values of L_η^* are around 1.2% at the
selected sections but increase to around 8.5% at selected instants, which may be ascribed to the
density of scattered measured data. However, the small values of L_η and close values of L_η^* in
Table IX also demonstrate the stage is predicted by FCNA and CNA to almost the same accuracy,
which further confirms that both algorithms can successfully deal with the complex flow and
sediment transport processes associated with contact discontinuities as they propagate over
irregular topographies.

Figure 12. Case 5: predicted (FCNA and CNA) and measured (Cao et al. 2011a) stage
hydrographs at four cross-sections for a channel flow induced by a landslide dam failure at
laboratory-scale.

Figure 13. Case 5: predicted (FCNA and CNA) water surface and bed profiles, and measured stage profiles (Cao et al. 2011a), at times (a) $t = 670$ s, (b) $t = 730$ s and (c) $t = 900$ s for channel flow induced by a landslide dam failure at laboratory-scale.

Table IX. L_{η}^* and L_{η} for Case 5 at selected instants and sections

L_{η}^* or L_{η}	$t = 670$ s	$t = 730$ s	$t = 900$ s	CS 1	CS 5	CS 8	CS 12
L_{η}^* of FCNA (%)	7.08	9.05	9.46	1.33	1.08	1.29	1.32
L_{η}^* of CNA (%)	7.26	8.62	9.59	1.15	0.74	1.00	1.03
L_{η} (%)	0.54	2.34	0.28	0.62	0.61	0.72	0.73

3.7 Discussion

The run time of the FCNA relative to its counterpart of the CNA for the test cases is listed in Table X. Although the run time of FCNA is relatively longer than that of the CNA, the differences between the two algorithms are within 10%. In connection to the issue of improving the computational efficiency, the technique of adaptive mesh refining can be incorporated, which has recently been found to be able to save the computational time significantly in computational river modelling (Huang et al. 2015).

In order to evaluate the possible conservation errors due to the equation manipulation in the CNA, the relative error of mass conservation R in the computational domain is deployed, which is defined as

$$R = \frac{abs[M_t - (M_0 + M_{in} - M_{out} + M_e)]}{M_t} \quad (32)$$

where M_0 , M_t = the mass of the water-sediment mixture flow at the initial state ($t = 0$) and at time $t > 0$; M_{in} , M_{out} = the mass of the inflow and outflow at the up- and downstream boundaries;

and M_e = the mass of bed erosion. The performance of the CNA in preserving mass conservation as well as the comparison with the FCNA is shown in the Table XI, with the values of R within 5×10^{-4} for Cases 1 to 4 and 5×10^{-2} for Cases 5. It is justified that mass conservation may not be perfectly satisfied as numerical errors are inevitable in practical numerical modelling, especially when wet-dry interfaces are involved. Although the FCNA generally gives a better performance than the CNA in preserving mass conservation over the range of test cases considered, the differences are limited. Therefore, the concern over conservation errors due to the equation manipulation of the CNA is no longer necessary.

Table X. Relative run time of test cases

Test case	1		2		3	4	5
	a	b	a	b			
Relative run time	1.070	1.072	1.09	1.04	1.08	1.05	1.04

Table XI. Relative mass conservation errors of test cases

R	1		2		3	4	5
	a	b	a	b			
R of FCNA	0.0	0.0	4.1×10^{-5}	4.6×10^{-4}	1.0×10^{-15}	7.4×10^{-6}	0.99×10^{-2}
R of CNA	0.0	0.0	4.3×10^{-5}	4.6×10^{-4}	4.2×10^{-5}	1.2×10^{-4}	1.14×10^{-2}

4. Conclusion

A numerical algorithm, FCNA, has been presented to directly solve the fully coupled SHSM equations with a non-capacity approach, based on an unmodified full conservation form of the equations with mixture density maintained on the LHS of the equation set. When implemented

1
2
3
4
5
6
7
8
9
10
11
12
13
14
15
16
17
18
19
20
21
22
23
24
25
26
27
28
29
30
31
32
33
34
35
36
37
38
39
40
41
42
43
44
45
46
47
48
49
50
51
52
53
54
55
56
57
58
59
60

with the well-balanced WSDGM version of the SLIC scheme, FCNA performed satisfactorily for the following series of test cases: steady equilibrium flow over a steep hump, density dam breaks with two discontinuities, dam breaks over erodible beds at prototype and laboratory scale, and a flood flow due to a landslide dam failure. It was demonstrated that the FCNA algorithm properly resolved complicated flows with sharp fronts (in stage and velocity), sediment transport processes with contact discontinuities over irregular topographies, and non-equilibrium bed morphological change. It was also found that the CNA, based on redistribution of the water-sediment mixture density term, achieved very similar accuracy to the FCNA over the range of verification and validation tests considered. Moreover, the relative run time was discussed and relative mass conservation errors of the two algorithms were compared, revealing the faster run time of the CNA and better performance of the FCNA in preserving mass conservation, but differences of the indexes between the two algorithms were subtle. These findings indicate that both the FCNA and CNA algorithms can be satisfactorily applied in computational river modelling.

Acknowledgements

The work reported in this manuscript is funded by Natural Science Foundation of China (Grants No. 51279144 and 11432015).

References

Aureli, F., Maranzoni, A. and Mignosa, P. (2004), “Two dimensional modeling of rapidly varying flows by finite volume schemes”, *Proceedings of the second international conference on fluvial hydraulics*, Balkema, Lisse, The Netherlands, pp. 837-847.

Aureli, F., Maranzoni, A., Mignosa, P. and Ziveri, C. (2008), “A weighted surface-depth gradient method for the numerical integration of the 2D shallow water equations with topography”, *Advances in Water Resources*, Vol. 31 No. 7, pp. 962-974.

- Batchelor, G. K. (1967), *An Introduction to Fluid Dynamics*, Cambridge University Press, England.
- Bellos, C. V., Soulis, V. and Sakkas, J. G. (1992), "Experimental investigation of two-dimensional dam-break induced flows", *Journal of Hydraulic Research*, Vol. 30 No. 1, pp. 47-63.
- Bermudez, A. and Vazquez, M.E. (1994), "Upwind methods for hyperbolic conservation laws with source terms", *Computers & Fluids*, Vol. 23 No. 8, pp. 1049-1071.
- Briganti, R., Torres-Freyermuth, A., Baldock, T.E., Brocchini, M., Dodd, N., Hsu, T.J., Jiang, Z., Kim, Y., Pintado-Patiño, J.C. and Postacchini, M. (2016), "Advances in numerical modelling of swash zone dynamics", *Coastal Engineering*, Vol. 115, pp. 26-41.
- Cao, Z., Pender, G., Wallis, S. and Carling, P. (2004), "Computational dam-break hydraulics over erodible sediment bed", *Journal of Hydraulic Engineering*, Vol. 130 No. 7, pp. 689-703.
- Cao, Z.X., Yue, Z.Y. and Pender, G. (2011a), "Landslide dam failure and flood hydraulics. Part I: experimental investigation", *Natural Hazards*, Vol. 59 No. 2, pp. 1003-1019.
- Cao, Z., Yue, Z.Y. and Pender, G. (2011b), "Landslide dam failure and flood hydraulics. Part II: coupled mathematical modelling", *Natural Hazards*, Vol. 59 No. 2, pp. 1021-1045.
- Cao, Z., Hu, P., and Pender, G. (2011c), "Multiple time scales of fluvial processes with bed load sediment and implications for mathematical modeling", *Journal of Hydraulic Engineering*, Vol. 137 No. 3, pp. 267-276.
- Cao, Z., Li, Z., Pender, G., and Hu, P. (2012), "Non-capacity or capacity model for fluvial sediment transport", *Water Management*, Proceedings of Institution of Civil Engineers, Vol. 165 No. 4, pp. 193-211.
- Cao, Z., Li, J., Pender, G. and Liu, Q. (2015), "Whole-process modeling of reservoir turbidity currents by a double layer-averaged model", *Journal of Hydraulic Engineering*, Vol. 141 No. 2, pp. 04014069.

- 616 Cao, Z., Hu, P., Pender, G., and Liu, H. (2016), "Non-capacity transport of non-uniform bed load
617 sediment in alluvial rivers", *Journal of Mountain Science*, Vol. 13 No. 3, pp.377-396.
- 618 Cao, Z., Xia, C., Pender, G. and Liu, Q. (2017), "Shallow water hydro-sediment-morphodynamic
619 equations for fluvial processes", *Journal of Hydraulic Engineering*, DOI:
620 [http://dx.doi.org/10.1061/\(ASCE\)HY.1943-7900.0001281](http://dx.doi.org/10.1061/(ASCE)HY.1943-7900.0001281).
- 621 Capart, H. and Young, D. L. (1998), "Formation of a jump by the dam-break wave over a granular
622 bed", *Journal of Fluid Mechanics*, Vol. 372, pp. 165-187.
- 623 Cea, L. and Vázquez-Cendón, M. E. (2010), "Unstructured finite volume discretization of two-
624 dimensional depth-averaged shallow water equations with porosity", *International Journal*
625 *for Numerical Methods in Fluids*, Vol. 63 No. 8, pp. 903-930.
- 626 Canestrelli, A., Dumbser, M., Siviglia, A., and Toro, E. F. (2010), "Well-balanced high-order
627 centered schemes on unstructured meshes for shallow water equations with fixed and mobile
628 bed", *Advances in Water Resources*, Vol.33 No.3, pp.291–303.
- 629 Fraccarollo, L. and Toro, E. F. (1995), "Experimental and numerical assessment of the shallow
630 water model for two-dimensional dam-break type problems", *Journal of Hydraulic Research*,
631 Vol. 33 No. 6, pp. 843-864.
- 632 Fraccarollo, L. and Capart, H. (2002), "Riemann wave description of erosional dam-break flows",
633 *Journal of Fluid Mechanics*, Vol. 461, pp. 183-228.
- 634 Gottlieb, S. and Shu, C. W. (1998), "Total variation diminishing Runge-Kutta schemes",
635 *Mathematics of computation*, Vol. 67 No. 221, pp. 73-85.
- 636 Guan, M., Wright, N., and Sleight, P. (2014). "2D process based morphodynamic model for
637 flooding by noncohesive dyke breach", *Journal of Hydraulic Engineering*, Vol. 140 No. 7, pp.
638 04014022.

- 639 Guan, M., Wright, N., Sleigh, P., and Carrivick, J. (2015). "Assessment of hydro-morphodynamic
640 modelling and geomorphological impacts of a sediment-charged jökulhlaup, at
641 Sólheimajökull, Iceland", *Journal of Hydrology*, Vol. 530, pp. 336-349.
- 642 Guan, M., Carrivick, J., Wright N., Sleigh, P., and Staines, K. (2016). "Quantifying the combined
643 effects of multiple extreme floods on river channel geometry and on flood hazards", *Journal*
644 *of Hydrology*, Vol. 538, pp. 256-268.
- 645 Harten, A., Lax, P. D. and van Leer, B. (1983), "On upstream differencing and Godunov-type
646 schemes for hyperbolic conservation laws", *SIAM Review*, Vol. 25 No. 1, pp. 35-61.
- 647 Hu, P. and Cao, Z. (2009), "Fully coupled mathematical modeling of turbidity currents over
648 erodible bed", *Advances in Water Resources*, Vol. 32 No. 1, pp. 1-15.
- 649 Hu, P., Cao, Z., Pender, G. and Tan, G. (2012), "Numerical modelling of turbidity currents in the
650 Xiaolangdi reservoir, Yellow River, China", *Journal of Hydrology*, Vol. 464-465, pp. 41-53.
- 651 Hu, P., Cao, Z., Pender, G. and Liu, H.H. (2014), "Numerical modelling of riverbed grain size
652 stratigraphic evolution", *International Journal of Sediment Research*, Vol.29 No. 3, pp. 329-
653 343.
- 654 Hu, P., Li, W., He, Z., Pährt, T. and Yue, Z. (2015), "Well-balanced and flexible morphological
655 modeling of swash hydrodynamics and sediment transport", *Coastal Engineering*, Vol. 96, pp.
656 27-37.
- 657 Huang, W., Cao, Z., Yue, Z., Pender, G. and Zhou, J. (2012), "Coupled modelling of flood due to
658 natural landslide dam breach", *Proceedings of the ICE - Water Management*, Vol. 165 No. 10,
659 pp. 525-542.
- 660 Huang, W., Cao, Z., Carling, P. and Pender, G. (2014), "Coupled 2D hydrodynamic and sediment
661 transport modeling of megaflood due to glacier dam-break in Altai Mountains, Southern
662 Siberia", *Journal of Mountain Science*, Vol. 11 No. 6, pp. 1442-1453.

1
2
3
4
5
6
7
8
9
10
11
12
13
14
15
16
17
18
19
20
21
22
23
24
25
26
27
28
29
30
31
32
33
34
35
36
37
38
39
40
41
42
43
44
45
46
47
48
49
50
51
52
53
54
55
56
57
58
59
60

663 Huang, W., Cao, Z., Pender, G., Liu, Q. and Carling, P. (2015). “Coupled flood and sediment
664 transport modelling with adaptive mesh refinement”, *Science China Technological Sciences*,
665 Vol. 58 No. 8, pp. 1425-1438.

666 Incelli, G., Dodd, N., Blenkinsopp, C.E., Zhu, F. and Briganti, R. (2016), “Morphodynamical
667 modelling of field-scale swash events”, *Coastal Engineering*, Vol.115, pp. 42-57.

668 Kim, D. H. (2015), “H2D morphodynamic model considering wave, current and sediment
669 interaction”, *Coastal Engineering*, Vol. 95, pp. 20-34.

670 Kim, J., Ivanov, V. Y. and Katopodes, N. D. (2013), “Modeling erosion and sedimentation
671 coupled with hydrological and overland flow processes at the watershed scale”, *Water
672 Resources Research*, Vol. 49 No. 9, pp. 5134-5154.

673 Leal, J. G. A. B., Ferreira, R. M. L. and Cardoso, A. H. (2006), “Dam-break wave-front celerity”,
674 *Journal of Hydraulic Engineering*, Vol. 132 No. 1, pp. 69-76.

675 Leighton, F. Z., Borthwick, A. G. L. and Taylor, P. H. (2010), “1-D numerical modelling of
676 shallow flows with variable horizontal density”, *International Journal for Numerical
677 Methods in Fluids*, Vol. 62 No. 11, pp. 1209-1231.

678 Li, S. and Duffy, C. J. (2011), “Fully coupled approach to modeling shallow water flow, sediment
679 transport, and bed evolution in rivers”, *Water Resources Research*, Vol. 47 No. 3, pp.
680 W03508.

681 Li, W., van Maren, D. S., Wang, Z. B., de Vriend, H. J. and Wu, B. (2014), “Peak discharge
682 increase in hyperconcentrated floods”, *Advances in Water Resources*, Vol. 67, pp. 65-77.

683 Liang, Q. (2010), “Flood simulation using a well-balanced shallow flow model”, *Journal of
684 Hydraulic Engineering*, Vol. 136 No. 9, pp. 669-675.

685 Liang, Q. and Borthwick, A. G. L. (2009), “Adaptive quadtree simulation of shallow flows with
686 wet-dry fronts over complex topography”, *Computers and Fluids*, Vol. 38 No. 2, pp. 221-234.

- 687 Liang, Q. and Marche, F. (2009), "Numerical resolution of well-balanced shallow water equations
688 with complex source terms", *Advances in Water Resources*, Vol. 32 No. 6, pp. 873-884.
- 689 Liska, R. and Wendroff, B. (1998), "Composite Schemes for Conservation Laws", *SIAM J. Numer.*
690 *Anal.*, Vol. 35 No. 6, pp. 2250-2271.
- 691 Pelosi, A., and Parker, G. (2014), "Morphodynamics of river bed variation with variable bedload
692 step length." *Earth Surface Dynamics*, Vol. 2, pp. 243-253.
- 693 Postacchini, M., Brocchini, M., Mancinelli, A., and Landon, M. (2012), "A multi-purpose, intra-
694 wave, shallow water hydro-morphodynamic solver", *Advances in Water Resources*, Vol. 38,
695 pp. 13-26.
- 696 Postacchini, M., Othman, I. K., Brocchini, M., and Baldock, T. E. (2014), "Sediment transport and
697 morphodynamics generated by a dam-break swash uprush: coupled vs uncoupled modeling",
698 *Coastal Engineering*, Vol. 89, pp. 99-105.
- 699 Qian, H., Cao, Z., Pender, G., Liu, H. and Hu, P. (2015), "Well-balanced numerical modelling of
700 non-uniform sediment transport in alluvial rivers", *International Journal of Sediment*
701 *Research*, Vol. 30 No. 2, pp. 117-130.
- 702 Qian, H., Cao, Z., Liu, H., and Pender, G. (2017). "Numerical modelling of alternate bar formation,
703 development and sediment sorting in straight channels." *Earth Surface Processes and*
704 *Landforms*, 42, 555–574. DOI: 10.1002/esp.3988.
- 705 Roe, P. L. (1981), "Approximate Riemann solvers, parameter vectors and difference schemes",
706 *Journal of computational physics*, Vol. 43 No. 2, pp. 357-372.
- 707 Rogers, B. D., Borthwick, A. G. L. and Taylor, P. H. (2003), "Mathematical balancing of flux
708 gradient and source terms prior to using Roe's approximate Riemann solver", *Journal of*
709 *Computational Physics*, Vol. 192 No. 2, pp. 422-451.

- 1
2
3 710 Rosatti, G. and Fraccarollo, L. (2006), "A well-balanced approach for flows over mobile-bed with
4 high sediment-transport", *Journal of Computational Physics*, Vol.220 No. 1, pp.312–338.
5 711
6
7 712 Simpson, G. and Castelltort, S. (2006), "Coupled model of surface water flow, sediment transport
8 and morphological evolution", *Computers & Geosciences*, Vol. 32 No. 10, pp. 1600-1614.
9 713
10
11 714 Spinewine, B. and Zech, Y. (2007), "Small-scale laboratory dam-break waves on movable beds",
12 *Journal of Hydraulic Research*, Vol. 45 No. sup1, pp. 73-86.
13 715
14
15 716 Toro, E. F. (1999), *Riemann solvers and numerical methods for fluid dynamics*, Springer-Verlag,
16 Germany.
17 717
18
19 718 Toro, E. F. (2001), *Shock-capturing methods for free-surface shallow flows*, John Wiley, England.
20
21
22 719 Toro, E. F., Spruce, M. and Speares, W. (1994), "Restoration of the contact surface in the HLL-
23 Riemann solver", *Shock waves*, Vol. 4, pp. 25-34.
24 720
25
26 721 Wu, W. (2007), *Computational river dynamics*, Taylor & Francis, London.
27
28
29 722 Wu, W. and Wang, S. S. Y. (2007), "One-dimensional modeling of dam-break flow over movable
30 beds", *Journal of Hydraulic Engineering*, Vol. 133 No. 1, pp. 48-58.
31 723
32
33 724 Wu, W. and Wang, S. S. Y (2008), "One-dimensional explicit finite-volume model for sediment
34 transport", *Journal of Hydraulic Research*, Vol. 46 No. 1, pp. 87-98.
35 725
36
37 726 Wu, W., Marsooli, R. and He, Z. (2012), "Depth-averaged two-dimensional model of unsteady
38 flow and sediment transport due to noncohesive embankment break/breaching", *Journal of*
39 *Hydraulic Engineering*, Vol. 138 No. 6, pp. 503-516.
40 728
41
42 729 Xia, J., Lin, B., Falconer, R. A. and Wang, G. (2010), "Modelling dam-break flows over mobile
43 beds using a 2D coupled approach", *Advances in Water Resources*, Vol. 33 No. 2, pp. 171-
44 183.
45 730
46
47
48
49
50
51
52
53
54
55
56
57
58
59
60

- 732 Xiao, H., Young, Y. L. and Prévost, J. H. (2010), "Hydro- and morphodynamic modeling of
733 breaking solitary waves over a fine sand beach. Part II: Numerical simulation", *Marine*
734 *Geology*, Vol. 269 No. 3-4, pp. 119-131.
- 735 Xie, J. ed. (1990), *River Modelling*, China Water and Power Press, Beijing (in Chinese).
- 736 Yue, Z., Cao, Z., Li, X. and Che, T. (2008), "Two-dimensional coupled mathematical modeling of
737 fluvial processes with intense sediment transport and rapid bed evolution", *Science in China*
738 *Series G: Physics Mechanics and Astronomy*, Vol. 51 No. 9, pp. 1427-1438.
- 739 Yue, Z., Liu, H., Li, Y., Hu, P. and Zhang, Y. (2015), "A well-balanced and fully coupled
740 noncapacity model for dam-break flooding", *Mathematical Problems in Engineering*, Vol.
741 2015, pp. 1-13.
- 742 Zech, Y., Soares-Fraza, S., Spinewine, B. and Grelle, N. L. (2008), "Dam-break induced
743 sediment movement: Experimental approaches and numerical modelling", *Journal of*
744 *Hydraulic Research*, Vol. 46 No. 2, pp. 176-190.
- 745 Zhang, S. and Duan, J. G. (2011), "1D finite volume model of unsteady flow over mobile bed",
746 *Journal of Hydrology*, Vol. 405 No. 1-2, pp. 57-68.
- 747 Zhou, J. G., Causon, D. M., Mingham, C. G. and Ingram, D. M. (2001), "The surface gradient
748 method for the treatment of source terms in the shallow-water equations", *Journal of*
749 *Computational Physics*, Vol. 168 No. 1, pp. 1-25.
- 750 Zhu, F. and Dodd, N. (2015), "The morphodynamics of a swash event on an erodible beach",
751 *Journal of Fluid Mechanics*, Vol. 762, pp. 110-140.

752
753
754 **Corresponding author**

755 Professor Zhixian Cao can be contacted at: zxcao@whu.edu.cn

1
2
3
4
5
6
7
8
9
10
11
12
13
14
15
16
17
18
19
20
21
22
23
24
25
26
27
28
29
30
31
32
33
34
35
36
37
38
39
40
41
42
43
44
45
46
47
48
49
50
51
52
53
54
55
56
57
58
59
60

756 **List of Tables**

757 **Table I.** Spatial increment and Courant number used in test cases

Test case	1	2	3	4	5
Spatial step Δx (m)	0.05	0.02	10	0.005	0.04
Courant number C_r	0.95	0.95	0.95	0.95	0.95

758

759

760 **Table II.** Summary of test cases

Test case	Sediment density ρ_s (kg/m ³)	Water density ρ_w (kg/m ³)	Gravitational acceleration g (m/s ²)	Sediment diameter d (mm)	Manning roughness n	Sediment porosity p
1	2,650	1,000	9.8	N/A	0.0	N/A
2	0.5&2.0	1.0	1.0	N/A	0.0	N/A
3	2,650	1,000	9.8	8.0	0.03	0.4
4*	1,540	1,000	9.8	3.5	0.025	0.3
5*	2,650	1,000	9.8	0.8	0.012	0.4

761 Notes: * Cases using measured data.

762

763

764 **Table III.** L_η^* for Case 1

L_η^* (%)	FCNA	CNA
Case 1a	0.0	0.0
Case 1b	0.0	0.0

765

766

767 **Table IV.** L_V^* for Case 2 at $t = 30$ s

Case	L_V^*	FCNA	CNA
Case 2a $\rho_{in} = 0.5 \text{ kg/m}^3$	L_η^* (%)	4.50	4.50
	L_u^* (%)	6.67	6.73
Case 2b $\rho_{in} = 2 \text{ kg/m}^3$	L_η^* (%)	2.48	2.49
	L_u^* (%)	4.44	5.85

768

769 **Table V.** L_V for Case 2 at selected instant and sections

Case	L_V	$t = 30 \text{ s}$	$x = 25 \text{ m}$	$x = 50 \text{ m}$	$x = 75 \text{ m}$
Case 2a $\rho_{in} = 0.5 \text{ kg/m}^3$	L_η (%)	0.002	0.0008	0.01	0.01
	L_u (%)	1.65	0.26	N/A	0.56
	L_c (%)	0.04	N/A	0.002	N/A
Case 2b $\rho_{in} = 2 \text{ kg/m}^3$	L_η (%)	0.02	0.016	0.02	0.015
	L_u (%)	3.25	3.26	N/A	0.07
	L_c (%)	0.016	N/A	0.00	N/A

770

771 **Table VI.** L_V^* for Case 3 at selected instants and sections

L_V^*	$t = 30 \text{ s}$	$t = 20 \text{ min}$	$x = 20 \text{ km}$	$x = 30 \text{ km}$
L_η^* of FCNA (%)	1.02	1.20	1.64	3.39
L_z^* of FCNA (%)	7.48	4.75	4.18	2.40
L_η^* of CNA (%)	0.90	1.17	1.66	3.41
L_z^* of CNA (%)	7.07	5.11	4.23	2.65

1
2
3
4
5
6
7
8
9
10
11
12
13
14
15
16
17
18
19
20
21
22
23
24
25
26
27
28
29
30
31
32
33
34
35
36
37
38
39
40
41
42
43
44
45
46
47
48
49
50
51
52
53
54
55
56
57
58
59
60

772 **Table VII.** L_V for Case 3 at selected instants and sections

L_V	$t = 30\text{ s}$	$t = 20\text{ min}$	$x = 20\text{ km}$	$x = 30\text{ km}$
L_η (%)	0.004	0.069	0.18	0.18
L_z (%)	0.63	0.57	0.18	0.48
L_u (%)	0.50	0.18	0.04	0.21
L_c (%)	1.29	0.72	0.16	0.53

773

774 **Table VIII.** L_V^* and L_V for Case 4 at selected instants and sections

L_V^* or L_V	$t = 0.505\text{ s}$	$t = 1.01\text{ s}$	$x = -0.05\text{ m}$	$x = 0.05\text{ m}$
L_η^* of FCNA (%)	7.43	8.79	N/A	N/A
L_η^* of CNA (%)	7.41	8.84	N/A	N/A
L_η (%)	0.09	0.20	1.90	1.90
L_z (%)	1.36	1.25	1.92	1.66
L_u (%)	0.36	0.44	0.89	0.94
L_c (%)	1.35	2.21	1.45	1.77

775

776 **Table IX.** L_η^* and L_η for Case 5 at selected instants and sections

L_η^* or L_η	$t = 670\text{ s}$	$t = 730\text{ s}$	$t = 900\text{ s}$	CS 1	CS 5	CS 8	CS 12
L_η^* of FCNA (%)	7.08	9.05	9.46	1.33	1.08	1.29	1.32
L_η^* of CNA (%)	7.26	8.62	9.59	1.15	0.74	1.00	1.03
L_η (%)	0.54	2.34	0.28	0.62	0.61	0.72	0.73

777

778 **Table X.** Relative run time of test cases

Test case	1		2		3	4	5
	a	b	a	b			
Relative run time	1.070	1.072	1.09	1.04	1.08	1.05	1.04

779

780 **Table XI.** Relative mass conservation errors of test cases

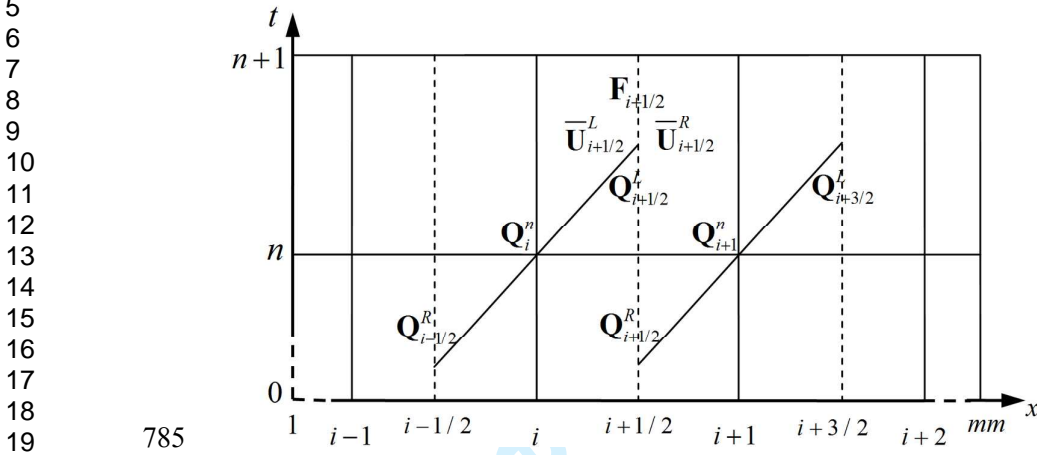
<i>R</i>	1		2		3	4	5
	a	b	a	b			
<i>R</i> of FCNA	0.0	0.0	4.1×10^{-5}	4.6×10^{-4}	1.0×10^{-15}	7.4×10^{-6}	0.99×10^{-2}
<i>R</i> of CNA	0.0	0.0	4.3×10^{-5}	4.6×10^{-4}	4.2×10^{-5}	1.2×10^{-4}	1.14×10^{-2}

781

782

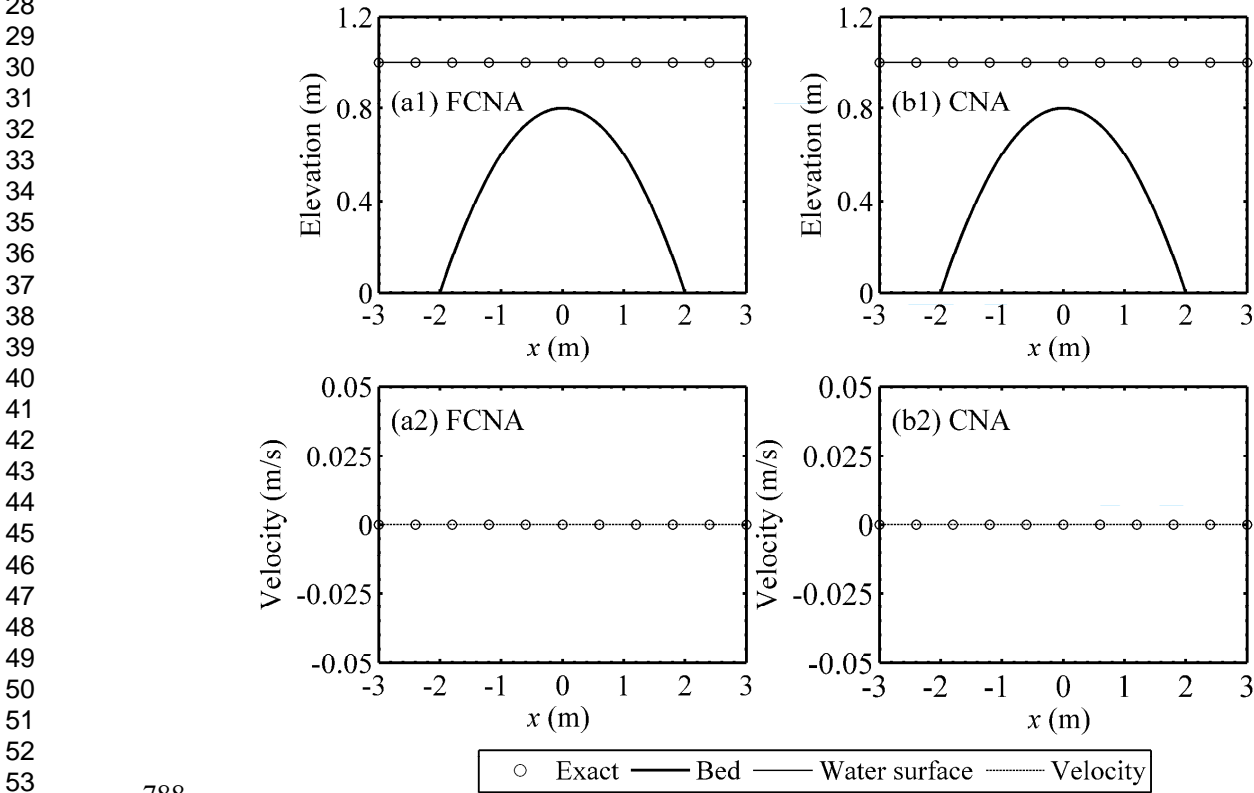
783

1
2
3 784 List of figure captions



20
21
22 786 Figure 1. Definition sketch of the WSDGM version of the SLIC scheme

23
24
25 787



54
55
56 789 Figure 2. Case 1a: equilibrium stage and velocity profiles predicted by FCNA and CNA for initial
57
58 790 stage of 1.0 m

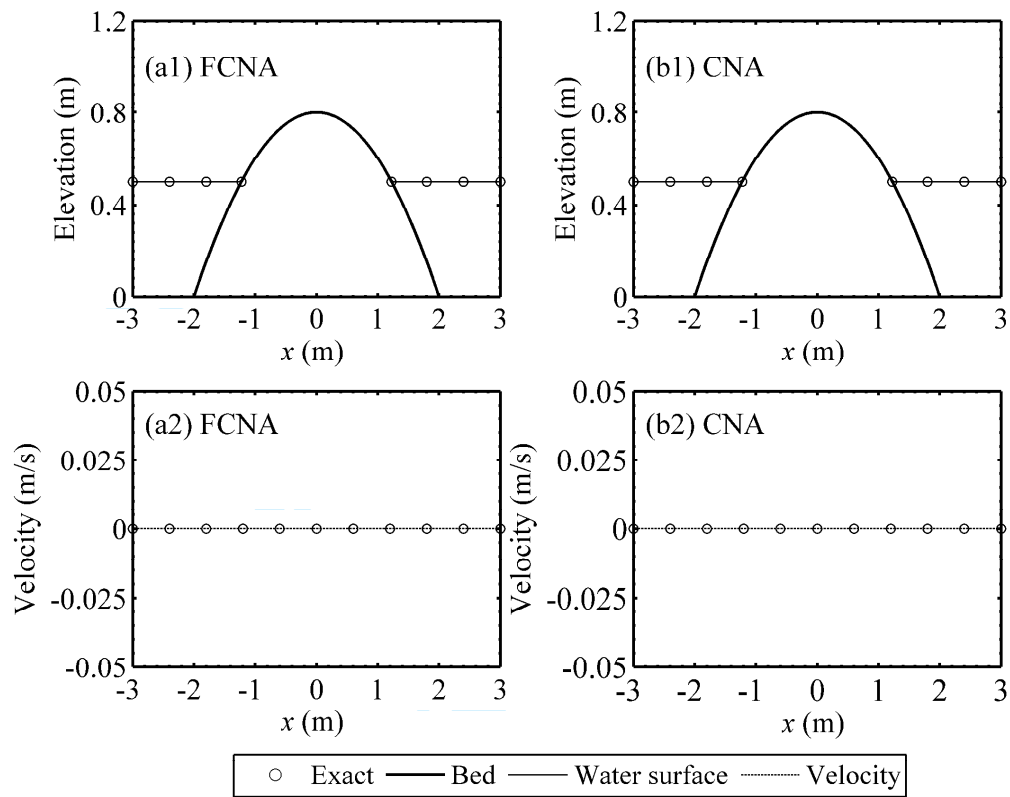


Figure 3. Case 1b: equilibrium stage and velocity profiles predicted by FCNA and CNA for initial stage of 0.5 m

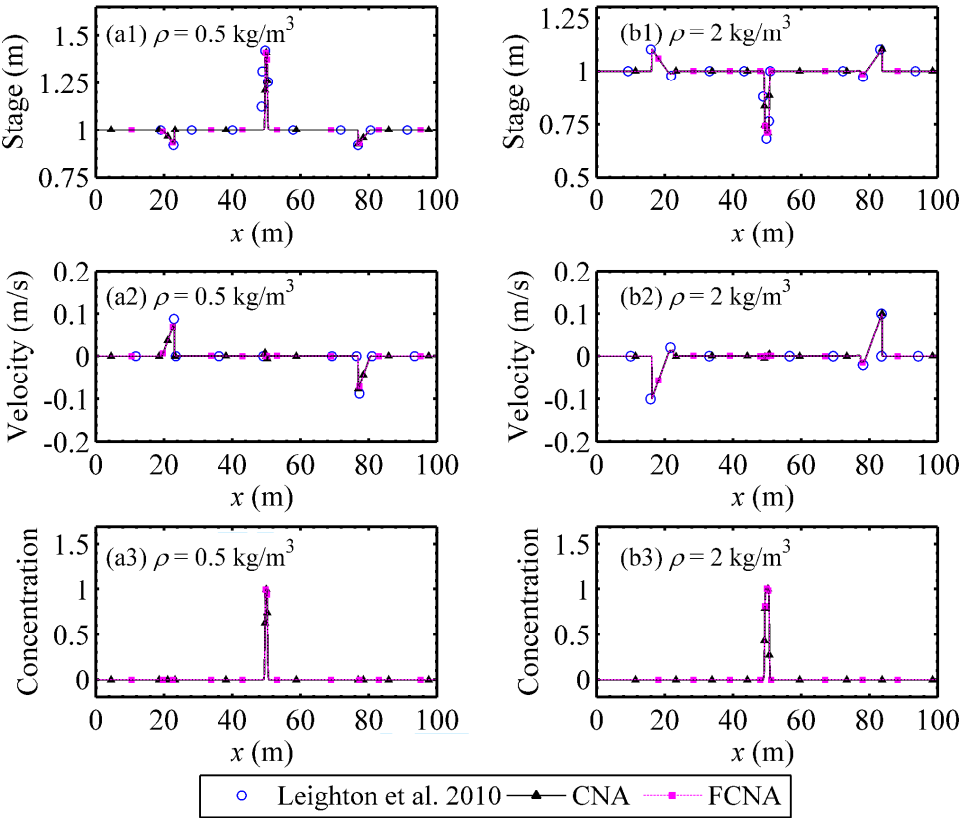


Figure 4. Case 2: computed stage, velocity and concentration profiles by FCNA and CNA and referenced stage and velocity profiles by Leighton et al. (2010) at $t = 30$ s for density dam break with two discontinuities for densities (a) $\rho = 0.5 \text{ kg/m}^3$ and (b) $\rho = 2 \text{ kg/m}^3$.

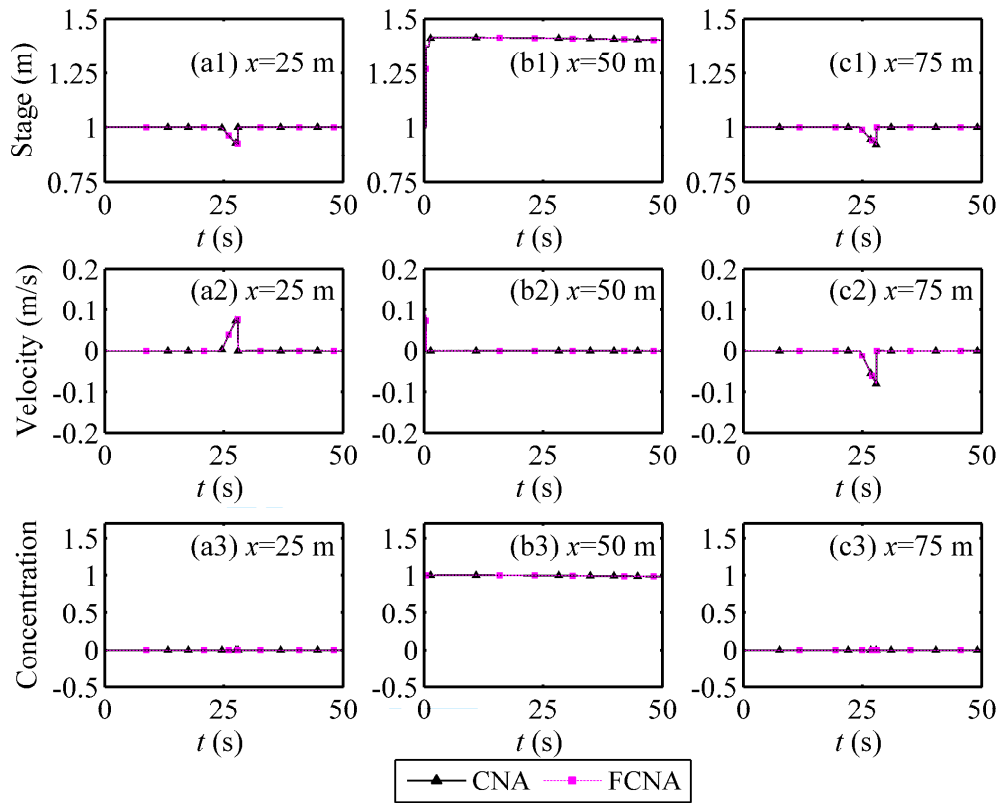


Figure 5. Case 2a: stage, velocity, and concentration time histories at locations (a) $x = 25$ m, (b) $x = 50$ m, and (c) $x = 75$ m, predicted by FCNA and CNA for density dam break ($\rho_{in} = 0.5$ kg/m³) with two discontinuities at times (a) $t = 30$ s and (b) $t = 20$ min.

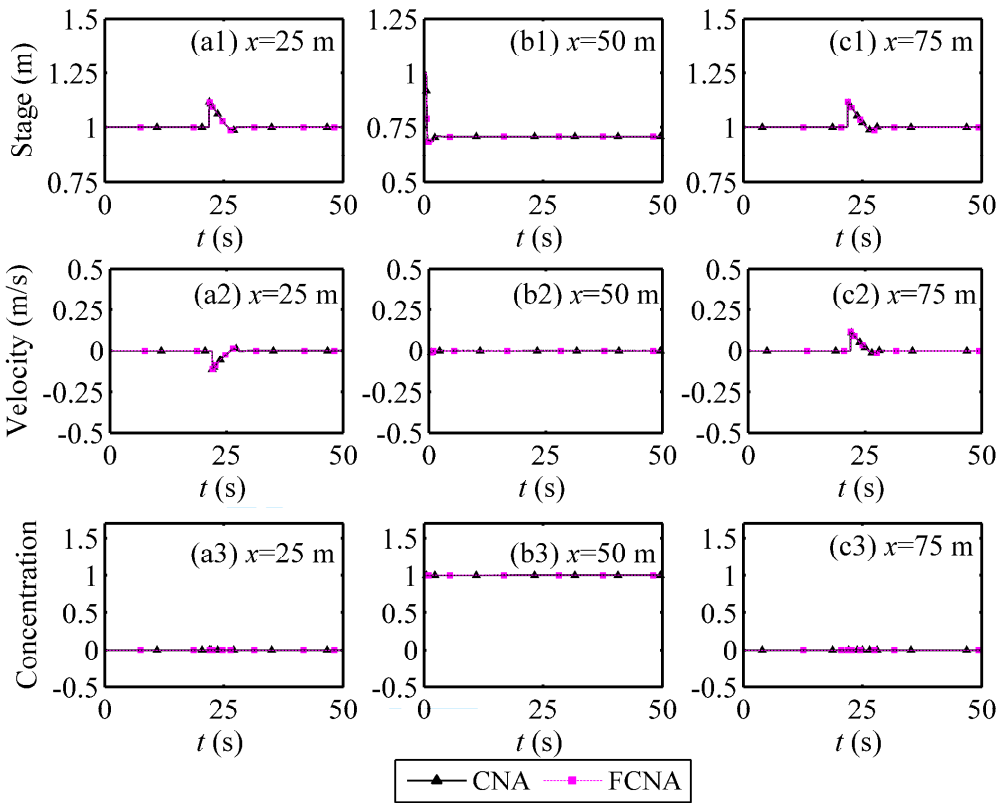


Figure 6. Case 2b: stage, velocity, and concentration time histories at locations (a) $x = 25$ m, (b) $x = 50$ m, and (c) $x = 75$ m, predicted by FCNA and CNA for density dam break ($\rho_{in} = 2.0$ kg/m³) with two discontinuities.

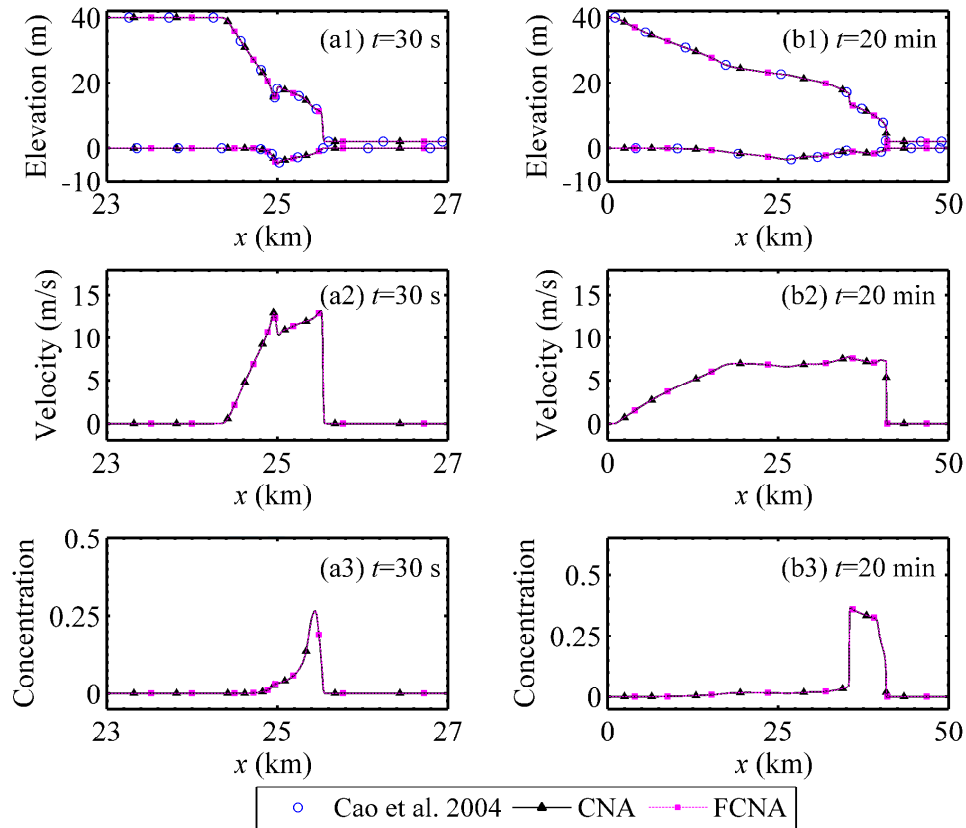


Figure 7. Case 3: dam break over an erodible bed at prototype scale: profiles of water surface and bed elevation, velocity, and concentration computed by FCNA and CNA and referenced stage and bed elevation predicted by Cao et al. (2004) at times (a) $t = 30$ s and (b) $t = 20$ min.

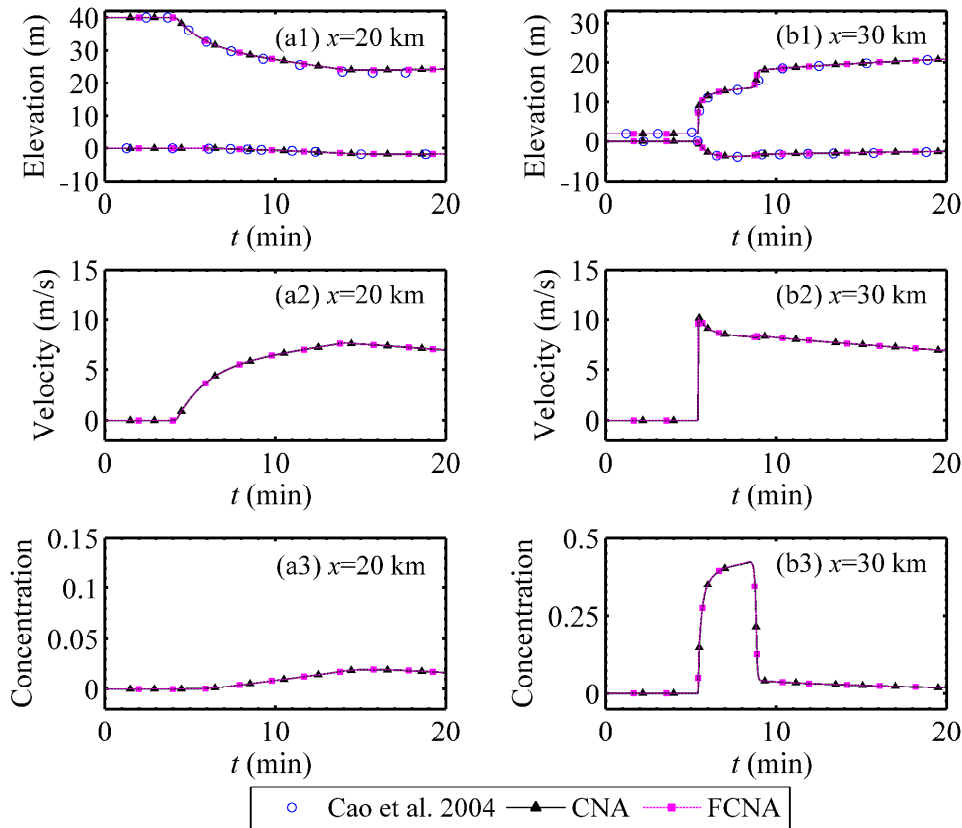


Figure 8. Case 3: dam break over an erodible bed at prototype scale: time histories of water surface and bed elevation, velocity, and concentration computed by FCNA and CNA and referenced stage and bed elevation predicted by Cao et al. (2004) at locations (a) $x = 20$ km and (b) $x = 30$ km.

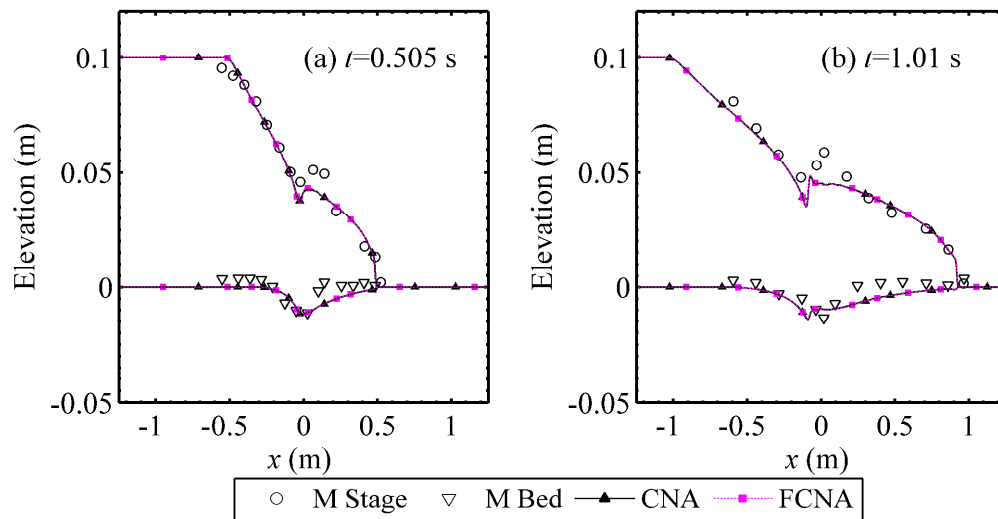


Figure 9. Case 4: computed (FCNA and CNA) and measured (Fraccarollo and Capart, 2002) water surface and bed elevation profiles at (a) $t = 0.505$ s and (b) $t = 1.01$ s for a dam break over an erodible bed.

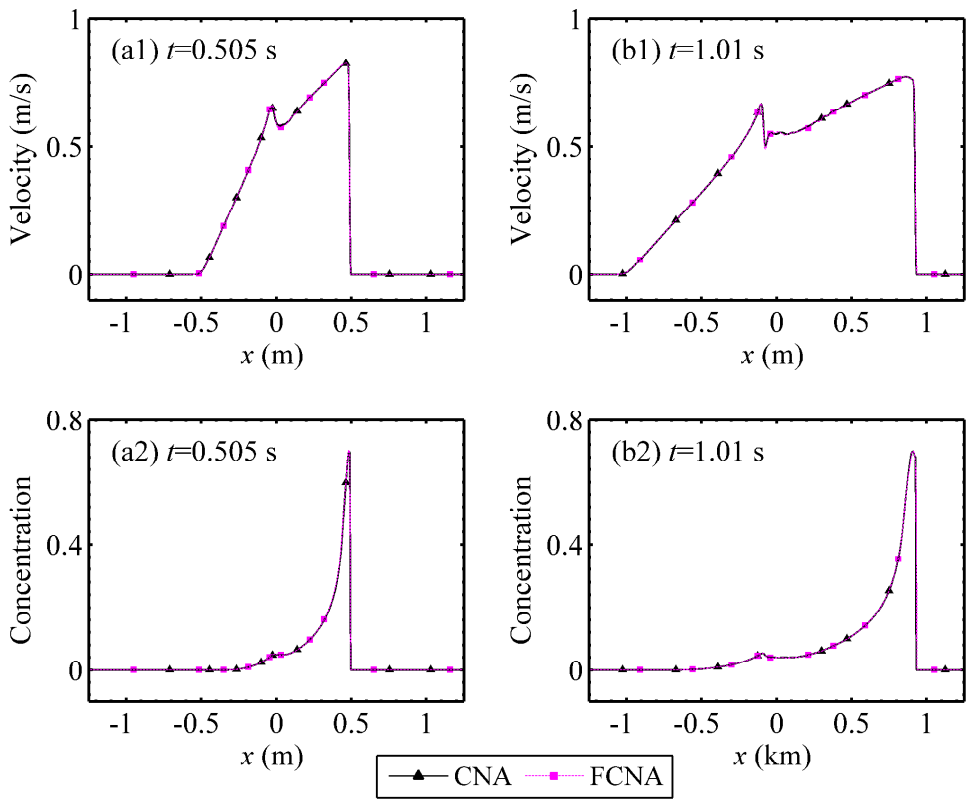


Figure 10. Case 4: computed (FCNA and CNA) velocity and concentration profiles at (a) $t = 0.505$ s and (b) $t = 1.01$ s for a dam break over an erodible bed.

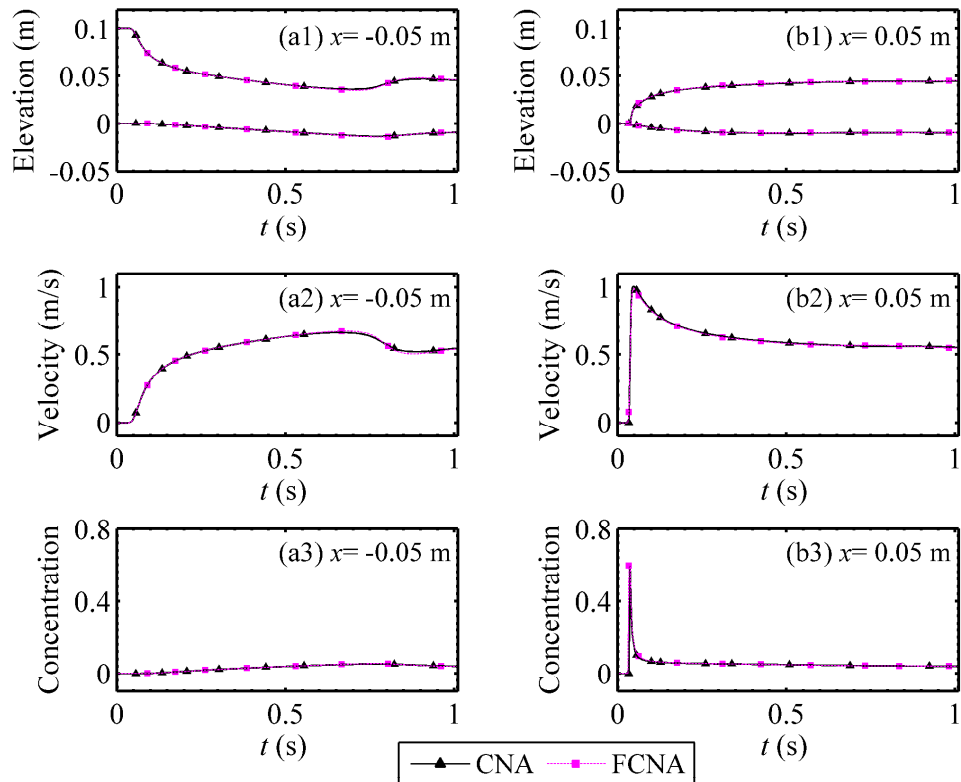


Figure 11. Case 4: computed (FCNA and CNA) water surface, bed elevation, velocity, and concentration time series at (a) $x = -0.05$ m and (b) $x = 0.05$ m for a dam break over an erodible bed.

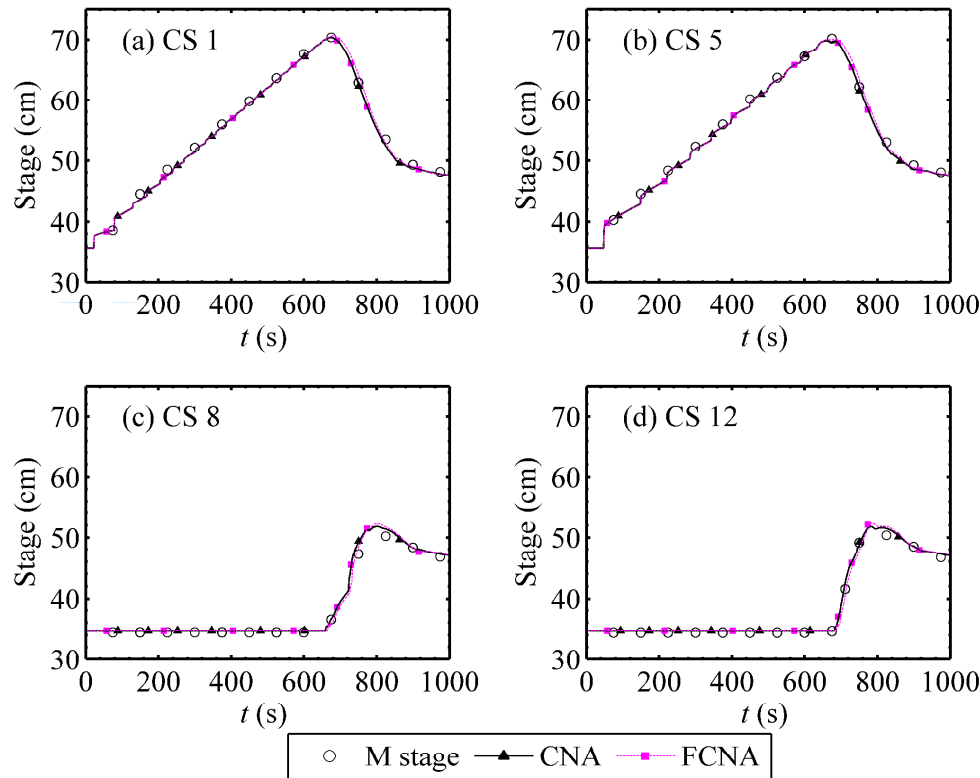


Figure 12. Case 5: predicted (FCNA and CNA) and measured (Cao et al. 2011a) stage hydrographs at four cross-sections for a channel flow induced by a landslide dam failure at laboratory-scale.

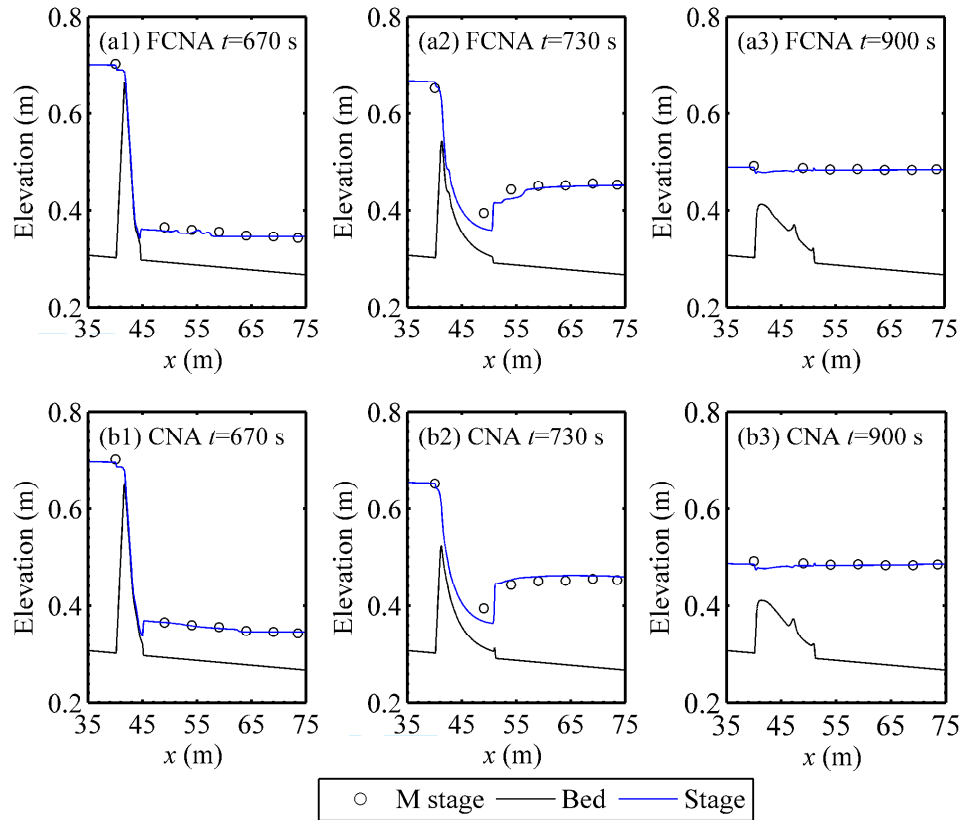
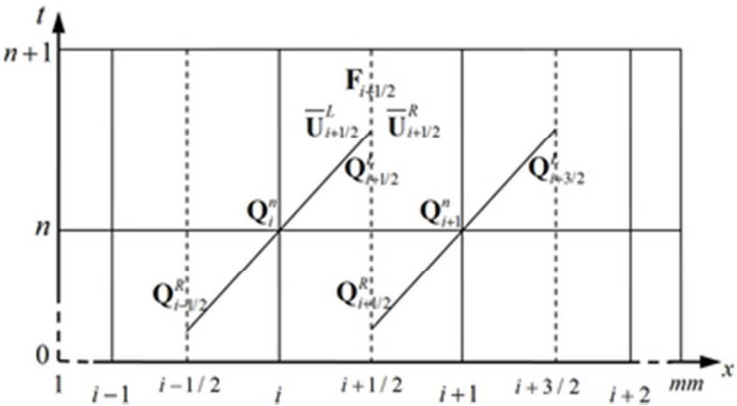
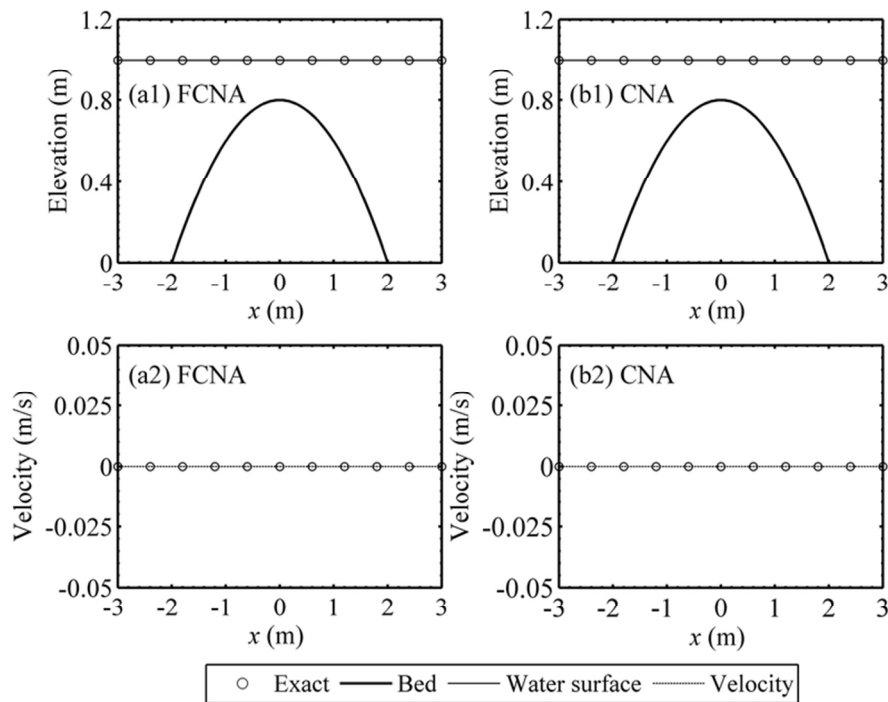


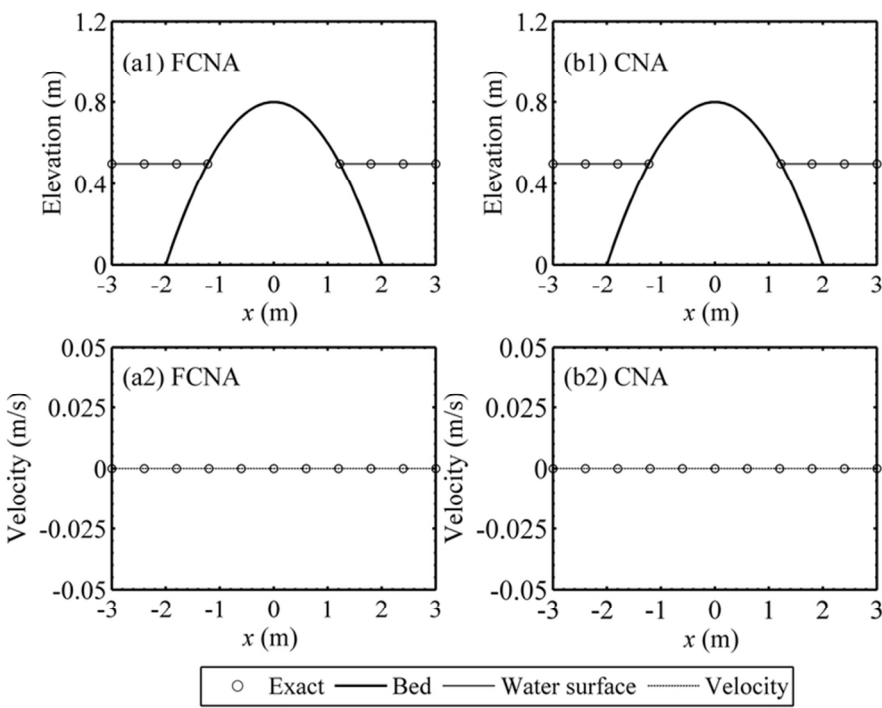
Figure 13. Case 5: predicted (FCNA and CNA) water surface and bed profiles, and measured stage profiles (Cao et al. 2011a), at times (a) $t = 670$ s, (b) $t = 730$ s and (c) $t = 900$ s for channel flow induced by a landslide dam failure at laboratory-scale.



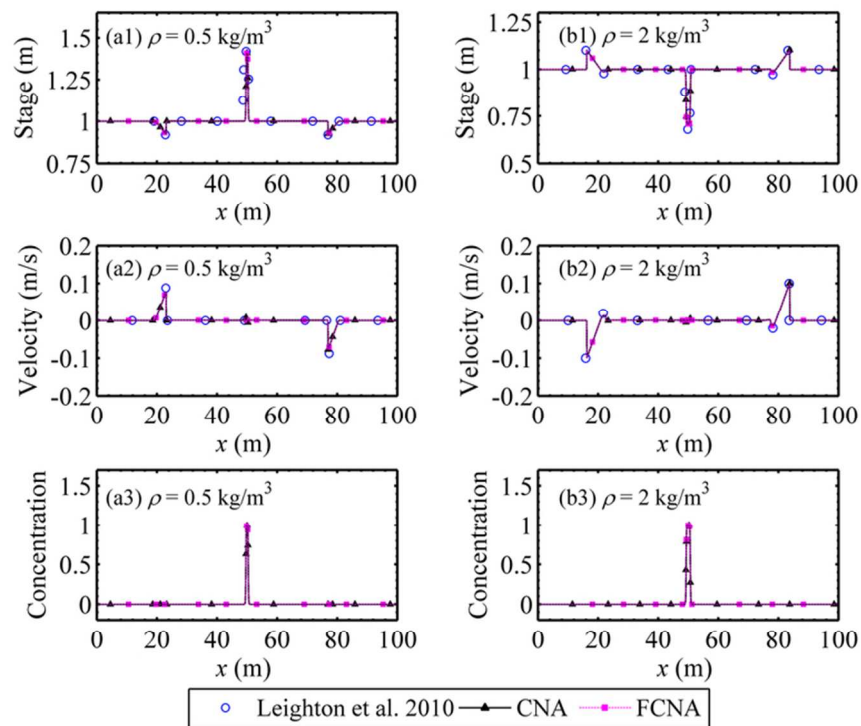
61x33mm (150 x 150 DPI)



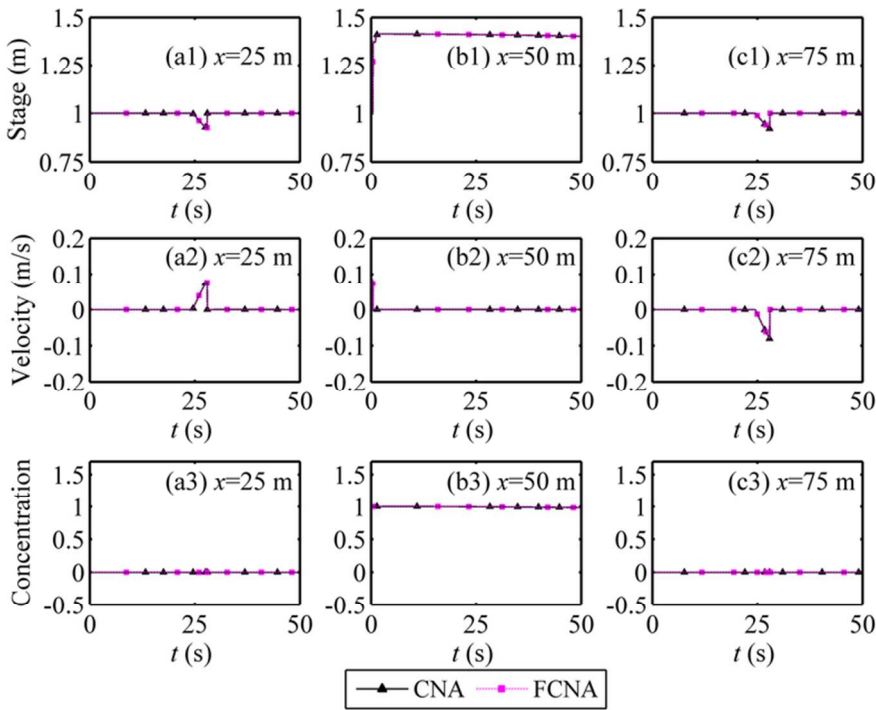
152x114mm (150 x 150 DPI)



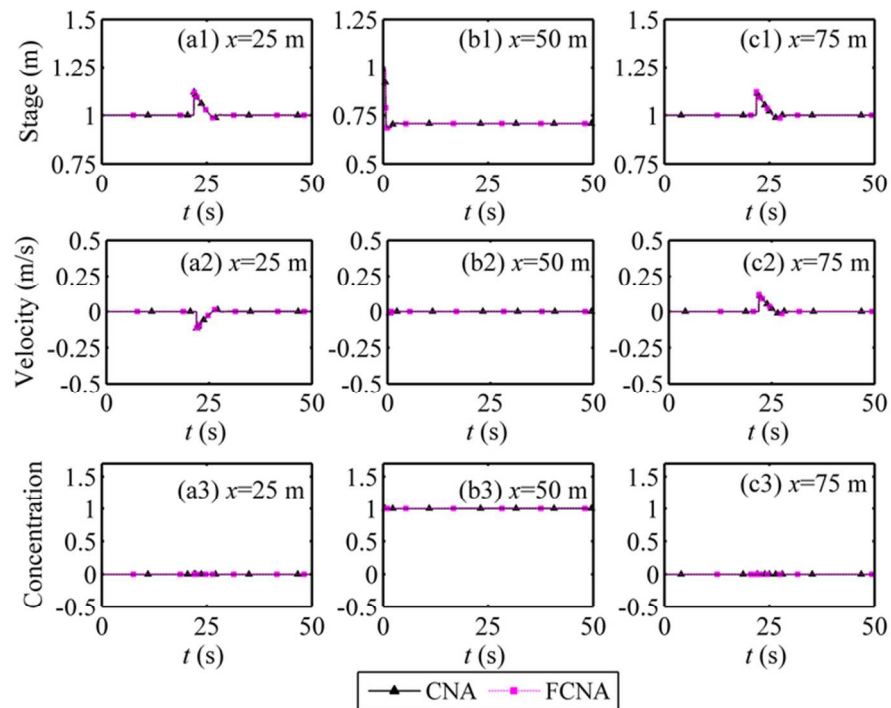
152x114mm (150 x 150 DPI)



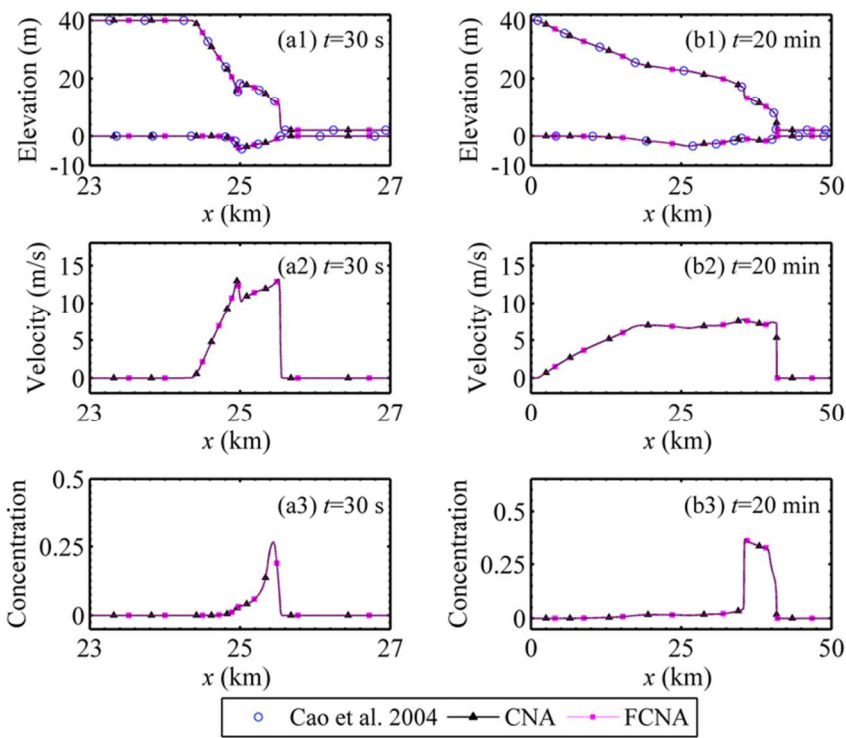
152x114mm (150 x 150 DPI)



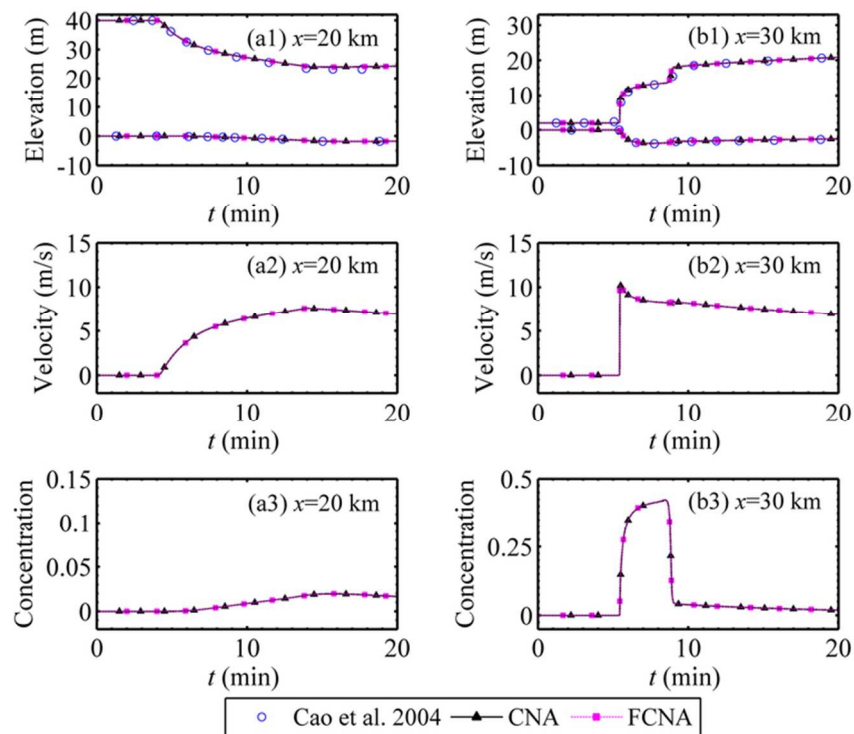
152x114mm (150 x 150 DPI)



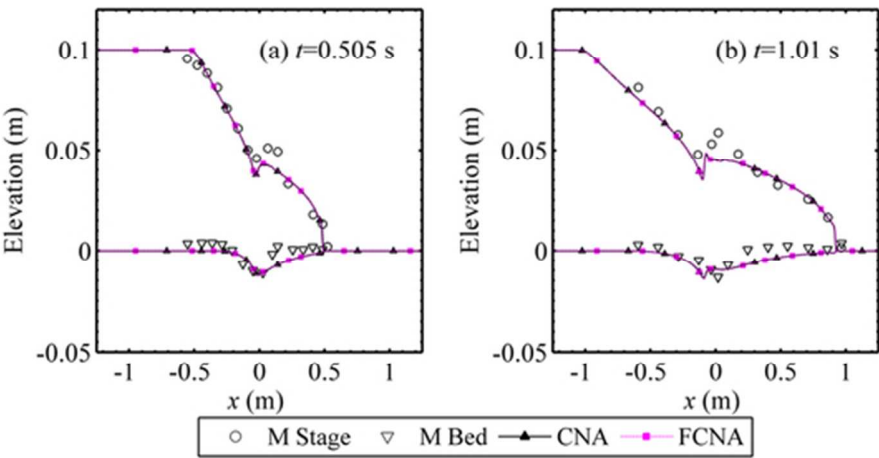
152x114mm (150 x 150 DPI)



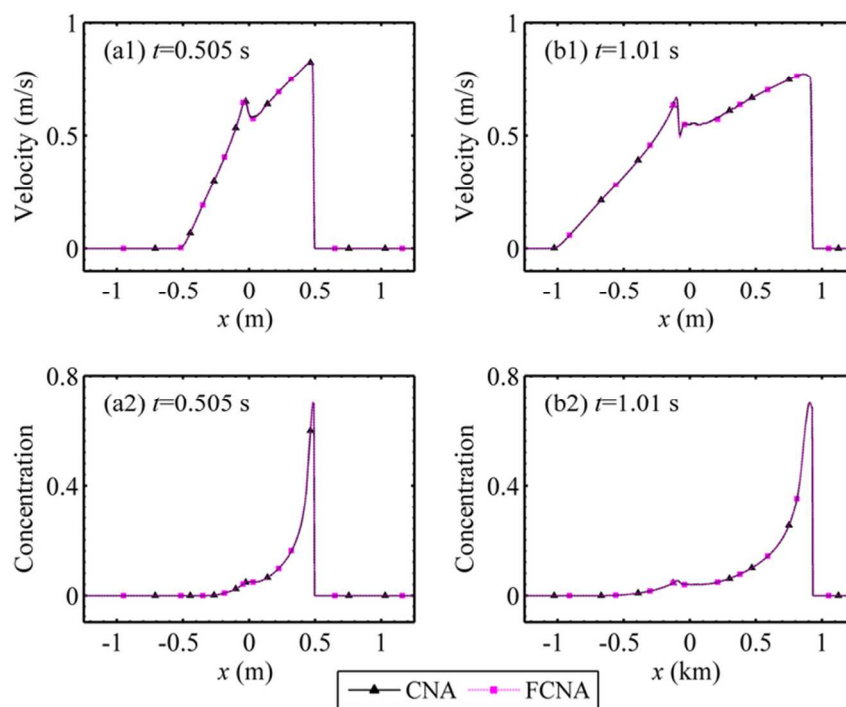
152x114mm (150 x 150 DPI)



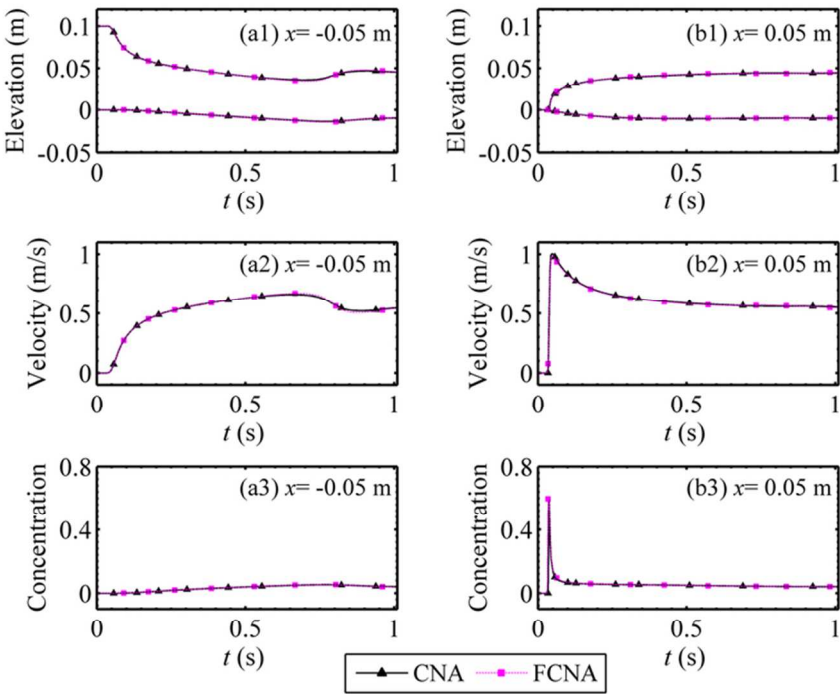
152x114mm (150 x 150 DPI)



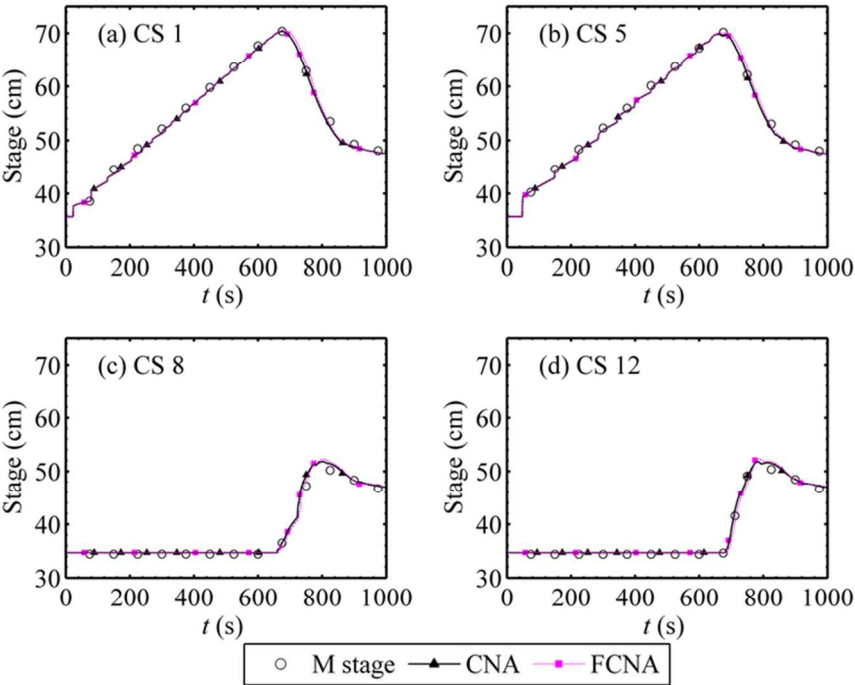
102x52mm (150 x 150 DPI)



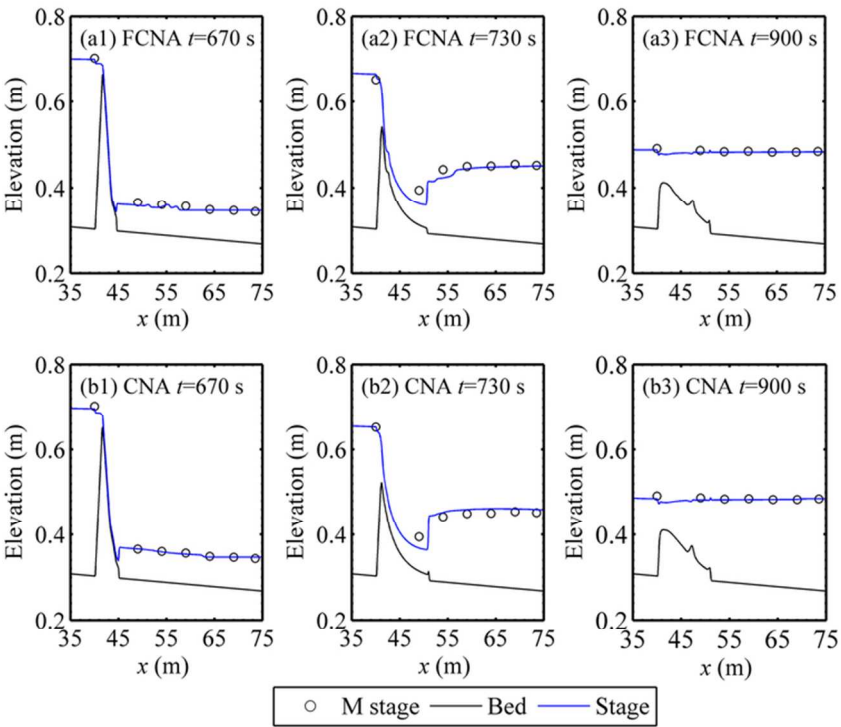
152x114mm (150 x 150 DPI)



152x114mm (150 x 150 DPI)



152x114mm (150 x 150 DPI)



152x114mm (150 x 150 DPI)

Reply to Review Comments

Title: *Numerical Algorithms for Solving Shallow Water Hydro-Sediment-Morphodynamic Equations*

Authors: Chunchen Xia, Zhixian Cao, Gareth Pender and Alistair G.L. Borthwick

Manuscript ID: EC-01-2016-0026R1

First of all, the authors very much appreciate the reviewer's comments and suggestions, and have carefully revised the manuscript. The following is written in response to the referees' comments. To help understand, **the Reply is set in blue**. In addition, other parts of the manuscript have also been modified, wherever appropriate.

To Referee 1

Comments:

Among the amendments/clarifications required in the first review, the authors were asked to simply underline numerical differences between their technique and that used in previous works (e.g., that of Hu et al., 2015). However, differently from what stated in the reply, I was not surprised at all about similarities with previous numerical models, and I only asked for a clarification. In summary: many words spent in the reply (first paragraph of the reply unnecessary), no trace of clarification in the text (though required). Hence, part of the second paragraph of the authors' reply must be used in the text to explain what required.

Reply: Thanks for the reviewer's suggestion. The clarification has been added when introducing how to compute the numerical fluxes and bed slope source term (Line193-199 in subsection 2.4.2).

1
2
3
4
5
6
7
8
9
10
11
12
13
14
15
16
17
18
19
20
21
22
23
24
25
26
27
28
29
30
31
32
33
34
35
36
37
38
39
40
41
42
43
44
45
46
47
48
49
50
51
52
53
54
55
56
57
58
59
60

Specific points

- L113-122: since the capacity/non-capacity issue is tackled in this paragraph, the authors should properly cite the works by Cao et al. (2012, 2016), which are referenced, but only cited at L463.

Reply: Yes, the references have been cited as suggested.

- L114: “Equally important”.

Reply: Yes, revised as suggested.

- L270: “then the latter is modified to be equal”.

Reply: Yes, revised as suggested.

Additional Questions:

1. Originality: Does the paper contain new and significant information adequate to justify publication?

Yes, it does.

Reply: Thanks for the positive comment.

2. Relationship to Literature: Does the paper demonstrate an adequate understanding of the relevant literature in the field and cite an appropriate range of literature sources? Is any significant work ignored?

Yes, it does.

Reply: Thanks for the positive comment.

1
2
3
4 3. Methodology: Is the paper's argument built on an appropriate base of theory, concepts, or
5
6 other ideas? Has the research or equivalent intellectual work on which the paper is based been well
7
8 designed? Are the methods employed appropriate?
9

10
11 Yes, it does.
12

13
14 **Reply:** Thanks for the positive comment.
15
16

17 4. Results: Are results presented clearly and analysed appropriately? Do the conclusions
18
19 adequately tie together the other elements of the paper?
20
21

22
23 Yes, it does.
24

25
26 **Reply:** Thanks for the positive comment.
27
28

29 5. Implications for research, practice and/or society: Does the paper identify clearly any
30
31 implications for research, practice and/or society? Does the paper bridge the gap between theory and
32
33 practice? How can the research be used in practice (economic and commercial impact), in teaching, to
34
35 influence public policy, in research (contributing to the body of knowledge)? What is the impact upon
36
37 society (influencing public attitudes, affecting quality of life)? Are these implications consistent with
38
39 the findings and conclusions of the paper?
40
41

42
43 Yes, it does.
44

45
46 **Reply:** Thanks for the positive comment.
47
48

49 6. Quality of Communication: Does the paper clearly express its case, measured against the
50
51 technical language of the field and the expected knowledge of the journal's readership? Has attention
52
53 been paid to the clarity of expression and readability, such as sentence structure, jargon use, acronyms,
54
55 etc.
56

57
58 Yes, it does.
59

60
Reply: Thanks for the positive comment.